Notch fatigue analysis and crack initiation life estimation of maraging steel fabricated by laser beam powder bed fusion under multiaixal loading

R. Branco[a,1], P.A. Prates[a], J.D. Costa[a], J.A. Martins Ferreira[a], C. Capela[b,a], F. Berto[c]

[a] University of Coimbra, CEMMPRE, Department of Mechanical Engineering, Coimbra, Portugal
[b] ESTG, Department of Mechanical Engineering, Instituto Politécnico de Leiria, Leiria, Portugal
[c] Department of Mechanical and Industrial Engineering, NTNU, 7491 Trondheim, Norway

Abstract

This paper deals with the notch fatigue behaviour and crack initiation life estimation in maraging steel fabricated by laser beam powder bed fusion under multiaxial loading. Tests are conducted in tubular geometries with lateral holes considering different normal stress to shear stress ratios and multiaxial loading levels. The cyclic stress-strain response at the notch-controlled process zone is simulated numerically using two alternative approaches: a generalised isotropic plasticity model with mixed isotropic-kinematic hardening, and a simple linear-elastic model. Both approaches demonstrated to be suitable for predicting the crack initiation sites, the directions of crack growth, and the fatigue life. Fatigue life was calculated from a SWT-based model combined with the Theory of Critical Distances. Elastic-plastic predictions led to smaller errors but slightly shifted to the non-conservative side.

Keywords: multiaxial fatigue, crack initiation, crack direction, cyclic plasticity, SWT damage parameter; maraging steel, powder bed fusion

1. Introduction

The development of reliable models for multiaxial fatigue life assessment is a complex task because, in general, there is a huge number of variables involved in the analysis [1-2]. The paradigm of additive manufacturing become this task more challenging and difficult once this new class of materials is more prone to fatigue failure [3-4]. Within the current additive manufacturing

[1] Corresponding author: R. Branco (ricardo.branco@dem.uc.pt)

processes, laser beam powder bend fusion is one of the most popular techniques. This process combines unique features with cost effectiveness, allowing the fabrication of functional parts in a layer-by-layer fashion directly from three-dimensional digital files. It is currently used in a number of high-value added industries, such as aeronautical, biomedical, automotive and moulds, among others [5-6].

Due to its martensitic matrix which requires a rapid quench from the austenitic region to temperatures below the martensitic start temperature, maraging steel is particularly suited for laser beam powder bed fusion, in particular for selective laser melting [7-8]. There are at least three reasons that may contribute to this success: (1) the small size of the melt pool and the associated high cooling rates; (2) the cyclic reheating during the printing process that may lead to the nucleation of hardening precipitates without heat treatments; and (3) the complex shapes and the limited number of parts required in the typical areas of application. One of the main drawbacks is its susceptibility to different types of anomalies (e.g. porosities, inclusions, lack of fusion, etc.) which may increase the uncertainty concerning the mechanical behaviour.

In the past few years, some effort has been put on the understanding of the mechanical behaviour, particularly on the triangular relationship between process parameters, microstructural features, and mechanical properties [9-11]. Although the research focused on monotonic and cyclic properties is relatively abundant, studies dealing with multiaxial fatigue of maraging steel fabricated by laser powder bed fusion are more limited [12]. A non-trivial problem in multiaxial fatigue is concerned with the accurate prediction of notch behaviour [13]. It requires not only the knowledge about the crack initiation sites and direction of crack growth, but also an accurate evaluation of cyclic plasticity at the geometric discontinuities [14].

Current strategies to deal with the cyclic plasticity response at the geometric discontinuities are usually materialised by means of experimental techniques, numerical methods, or approximate solutions [15]. Experimental techniques, due to their intrinsic nature, have some limitations, such as the difficulty to assess complicated geometric details or the impossibility to analyse the stress-strain fields inside the body [16]. On the other hand, with the advent of computer technology, numerical methods can provide precise results even for complex details, provided that an

adequate constitutive model is implemented. Nevertheless, constitutive relationships for additively manufactured maraging steel have only been derived for uniaxial loading [17-18].

Regarding the multiaxial fatigue life prediction, different models can be used. Within the most successful approaches, we can mention those that reduce the multiaxial stress-stress state to an equivalent uniaxial state [19-22]. In general, this link is formalised through a representative fatigue damage parameter, which can be expressed in terms of stress-based, strain-based, or energy-based relationships. The comparison between the equivalent fatigue damage quantifier and the uniaxial fatigue response allows to define the associated fatigue lifetime. Therefore, in order to develop reliable models for multiaxial fatigue life assessment of maraging steels fabricated by laser beam powder bed fusion, it is necessary to identify representative fatigue damage quantifiers.

This paper aims to address the above-mentioned gaps. Firstly we conduct a series of experimental tests in tubular geometries with lateral holes fabricated by laser beam powder bed fusion subjected to proportional bending-torsion loading. Then, it is implemented a generalised isotropic plasticity model with mixed isotropic-kinematic hardening to simulate the cyclic stress-strain response at the notch-affected zone. A uniaxial equivalent model formulated using a SWT-based quantifier is successfully developed to assess the fatigue lifetime. After that, numerical predictions of fatigue crack initiation, direction of fatigue crack initiation, and fatigue lifetime are compared to those obtained experimentally, and with those obtained with a simple linear-elastic model.

2. Experimental procedure

The specimen geometry used in the multiaxial fatigue tests, which consists of a 3mm-thick tubular configuration with a length of 150 mm and an outer diameter of 16 mm, is presented in Figure 1. It was fabricated vertically, from 18Ni300 maraging steel, using a Concept Laser M3 linear printing system equipped with a 400W Nd:YAG fibre laser. Each layer was created with a constant thickness of 40 μm, a scan speed of 200 mm/s, and a hatch spacing of 100 μm. The average surface roughness of the as-built samples was equal to 12 μm. After the additive manufacturing process, the 5mm-diameter hole was drilled by CNC, and the outer surface of the samples was machined and polished to a scratch-free condition. The final surface roughness of the outer surface was 0.5 μm. The main mechanical properties are listed in Table 1.

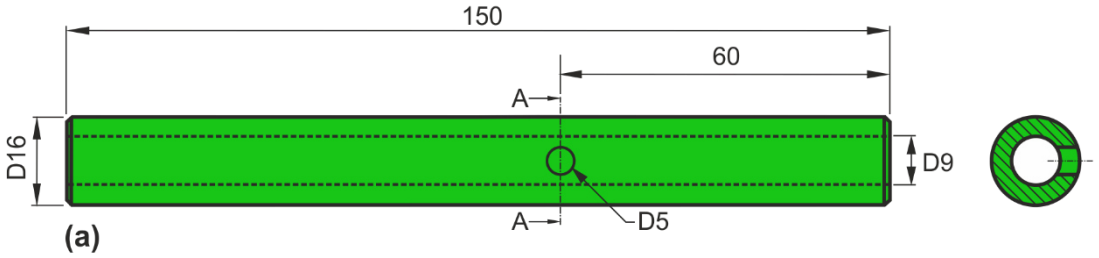

Figure 1. Specimen geometry of additively used in the multiaxial fatigue tests (units: mm).

The bending-torsion tests were performed under in-phase constant-amplitude loading in a conventional servo-hydraulic machine connected to a custom-made gripping system with a stress ratio (R) equal to 0. Three normal stress to shear stress ratios (σ/τ) were considered, namely σ/τ = 4, σ/τ = 2, and σ/τ = 4/3. The nominal normal stresses applied in the notched region are listed in Table 2. The notch region was monitored in situ to detect the crack initiation sites and to track the crack paths along the external surface of the specimen. The crack initiation lives, listed in Table 2, were calculated in a previous paper published by the authors [12] for a crack size equal to the fatigue characteristic length (a_0) defined from the El-Haddad parameter. Under pulsating loading conditions, a_0 = 121 μm [12].

Table 1. Mechanical properties of the additively manufactured 18Ni300 maraging steel.

Property	Value
Porosity (%)	0.74±0.09
Density (g/m^3)	7.42
Hardness (HV1)	354±5
Tensile strength (MPa)	1147±13
Yield strength (MPa)	910±11
Strain at failure (%)	5.12±0.001
Fatigue limit stress range, $\Delta\sigma_0$ (MPa)	266
Stress intensity factor range threshold, ΔK_{th0} (MPa·m$^{0.5}$)	5.2
Cyclic hardening coefficient, K' (MPa)	1921.2
Cyclic hardening exponent, n'	0.110

Table 2. Summary of multiaxial fatigue tests.

Loading case	1	2	3	4	5	6	7	8
σ/τ	4	4	4	2	2	2	4/3	4/3
σ_a (MPa)	78.3	79.6	95.5	66.3	79.6	95.5	55.3	79.6
σ_m (MPa)	86.1	87.6	105.1	73.0	87.6	105.1	60.8	87.6
N_i (cycles)	35,115	75,516	20,037	52,883	32,677	7947	84,204	8514

3. Numerical modelling

In this study, two constitutive models were developed: a linear-elastic, and an elastic-plastic. The former was modelled by the generalised Hooke's law, assuming a continuous, homogeneous, and isotropic behaviour. Regarding the latter, the elastic regime was also modelled via the generalised Hooke's law and the plastic regime was modelled by the von Mises yield criterion coupled with a mixed isotropic-kinematic hardening law under an associated flow rule, as follows:

$$\mathrm{f}(\sigma' - \mathrm{X}) - \mathrm{Y} \leq 0 \tag{1}$$

where $\mathrm{f}(\sigma' - \mathrm{X})$ represents the von Mises yield criterion, σ' is the deviatoric Cauchy stress tensor, X is the backstress tensor (described by the kinematic hardening law) and Y is the yield stress (described by the isotropic hardening law). For the maraging steel manufactured by laser beam powder bed fusion, Y was modelled using a Voce isotropic hardening law, i.e.

$$\mathrm{Y} = \mathrm{Y}_0 + (\mathrm{Y}_{\mathrm{sat}} - \mathrm{Y}_0)[1 - \exp(-\mathrm{C}_{\mathrm{Y}}\bar{\varepsilon}^{\mathrm{p}})] \tag{2}$$

where Y_0, $\mathrm{Y}_{\mathrm{sat}}$, and C_{Y} are material parameters and $\bar{\varepsilon}^{\mathrm{p}}$ is the equivalent plastic strain. The same hardening law was used to model the material behaviour of the conventional 34CrNiMo6 high-strength steel used in the gripping system, which was included in the numerical model to simulate as close as possible the experimental tests.

The non-linear kinematic hardening of both materials was modelled by means of an Armstrong-Frederick law:

$$\dot{\mathrm{X}} = \mathrm{C}_{\mathrm{X}}\left[\frac{\mathrm{X}_{\mathrm{sat}}}{\bar{\sigma}}(\sigma' - \mathrm{X}) - \mathrm{X}\right]\dot{\bar{\varepsilon}}^{\mathrm{p}} \tag{3}$$

where $\dot{\mathrm{X}}$ is the backstress rate, C_{X}, and $\mathrm{X}_{\mathrm{sat}}$ are material parameters, $\bar{\sigma}$ is the equivalent stress, and $\dot{\bar{\varepsilon}}^{\mathrm{p}}$ is the equivalent plastic strain rate. The determination of the material

constants that best described the cyclic elastic-plastic behaviour of both steels was carried out by minimising the function:

$$F(A) = \sum_{i=1}^{N} \left(\frac{\sigma^{Num}(A) - \sigma^{Exp}}{\sigma^{Exp}} \right)_i^2 \quad (4)$$

where $\sigma^{Num}(A)$ and σ^{Exp} are the analytical fitted and the experimentally measured values of true stress at point i (which corresponds to a given equivalent plastic strain value), N is the total number of experimental data points, and A is the set of material parameters to be identified.

The fitting procedure for the additively manufactured 18Ni300 maraging steel was carried out using stress-strain data collected in a low-cycle fatigue test performed under strain-controlled conditions with a strain amplitude ($\Delta\varepsilon/2$) of ±0.8% [23]. The material constants were determined using 6600 points which correspond to the first 33 cycles, i.e. 80% of the total life. Figure 2(a) compares the simulated cyclic stress-strain response with the hysteresis loops at the mid-life cycle. Overall, there is an excellent correlation between the numerical and the experimental results which is an excellent outcome. In relation to the 34CrNiM6 high-strength steel, the fitting process has been successfully done in a previous study for a strain amplitude of ±2.0% (see Figure 2(b)) and the numerical results are very good agreement with the experimental data [24]. The fitted constants for both materials are summarised in Table 3.

Table 2. Fitted elastic-plastic parameters for the simulated materials.

Material	Hooke law		Voce law		Armstrong-Frederick law		
	E (GPa)	ν	Y_0 (MPa)	Y_{sat} (MPa)	C_Y	Cx	X_{sat} (MPa)
18Ni300	168.0	0.330	683.62	683.62	0	728.34	402.06
34CrNiMo6	209.8	0.296	741.51	741.51	0	87.60	212.16

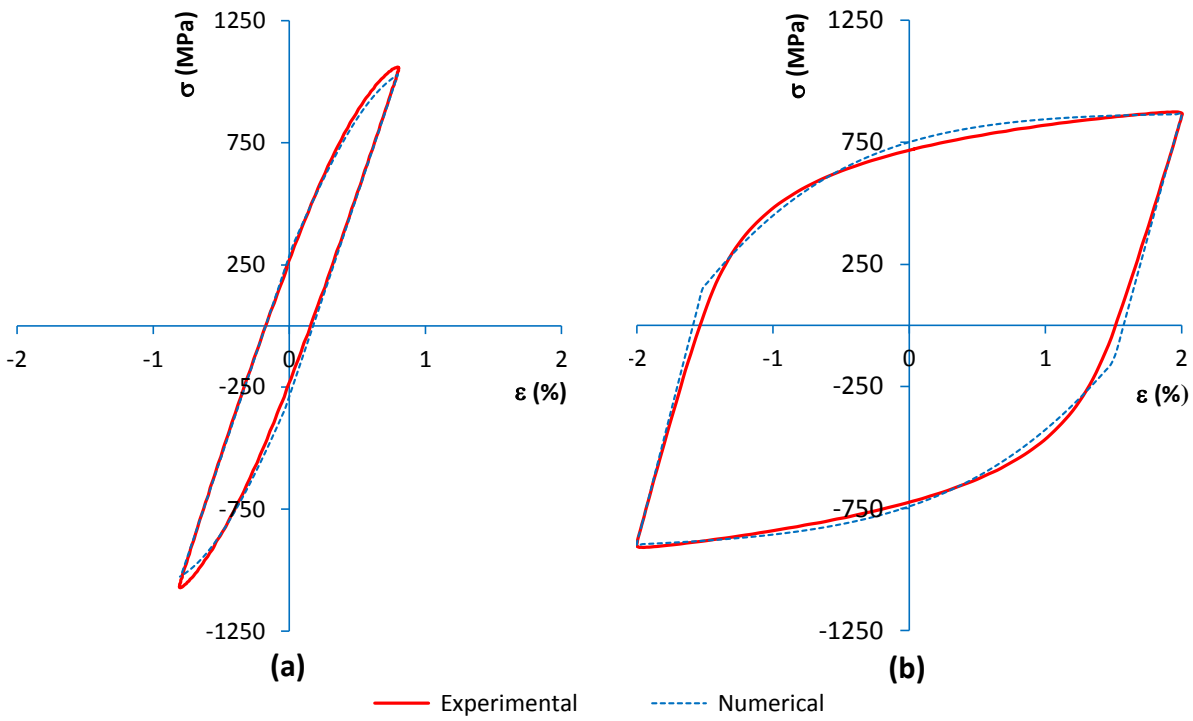

Figure 2. Simulated and experimental stress-strain hysteresis loops for the: (a) additively manufactured 18Ni300 maraging steel manufactured at $\Delta\varepsilon/2 = \pm 0.8\%$; and (b) conventional 34CrNiMo6 high-strength steel at $\Delta\varepsilon/2 = \pm 2.0\%$. Experimental cycles refer to the hysteresis loop collected at the mid-life.

Figure 3 shows the finite element model used in this study. As can be seen, it includes the specimen geometry, represented in green, and a prismatic bar, part of the gripping system, connected to the end of the specimen, represented in purple. The material of the specimen was modelled using the material constants of the additively manufactured 18Ni300 maraging steel, and the material of the prismatic bar was modelled using the material constants of the conventional 34CrNiMo6 high-strength steel. DD3Imp, an implicit three-dimensional finite element code developed at the University of Coimbra, was used to perform the numerical simulations [25-26].

The mesh was created in a parametric framework with 8-node isoparametric brick elements, and its density resulted from a trade-off between computational overhead and accuracy. At the geometric discontinuity, an ultrafine mesh was created to evaluate the higher stress-strain gradients that are expected to occur in that region. On the contrary, in the regions further from

the hole, the element size was increased to reduce the simulation time. The assembled model had 152,248 elements and 163,138 nodes, while the refined region around the hole contained 43,000 elements and 48,000 nodes, respectively.

In order to replicate as close as possible the experimental tests, the normal stress to shear stress ratio acting on the notch region was generated from a single force, F, applied on the external prismatic bar connected to the specimen. The outer surface of the other end was fixed for an extension of 30 mm. The magnitude of the force (F) and its point of application (h) were defined in a case-by-case basis. In all simulations, L was fixed. The loading was applied during five cycles, comprising both loading and unloading events, to obtain a stabilised cyclic elastic-plastic response. The stress and strain fields of the last cycle were used in the fatigue analysis.

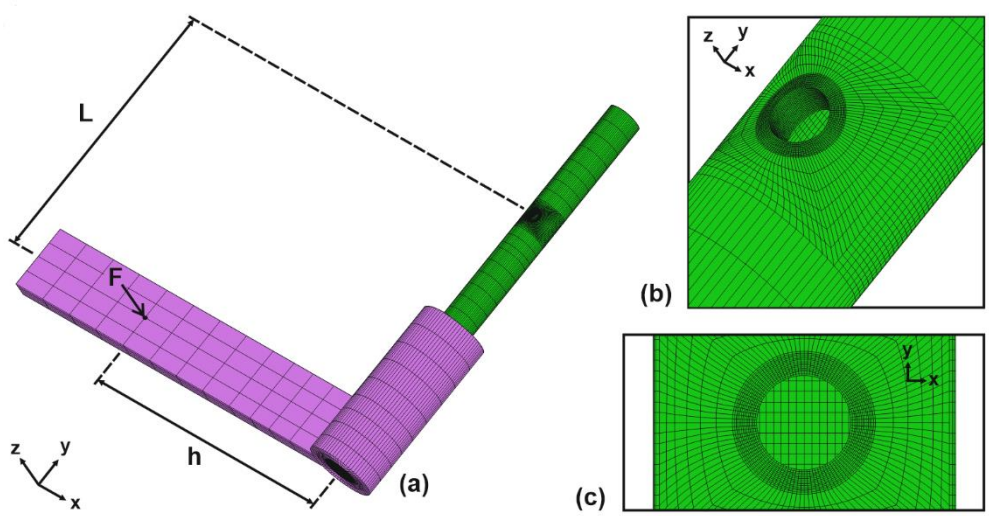

Figure 3. Finite element model used in the linear-elastic and elastic-plastic numerical simulations: (a) assembled model; and (b,c) details of the notch region (green: additively manufactured maraging steel; purple: conventional high-strength steel).

4. Results and discussion

4.1 Notch fatigue behaviour

The notch fatigue behaviour was governed by the normal stress to shear stress ratio (σ/τ). Figure 4 exhibits the typical fatigue crack initiation sites and the fatigue crack angles observed in the experiments at the outer surface of the specimen. The measured values and the numerical predictions are summarised in Table 4. Regardless of the loading case, two cracks have initiated in diametrically opposite points of the hole. These locations tend to be

closer to the longitudinal central plane, represented by the thicker white line, as the σ/τ ratio decreases. Lower σ/τ ratios increase the shear stress level leading to higher degrees of mixed mode loading. Such behaviour is in line with that reported in the literature for thin-walled geometries subjected to multiaxial loading [27-28].

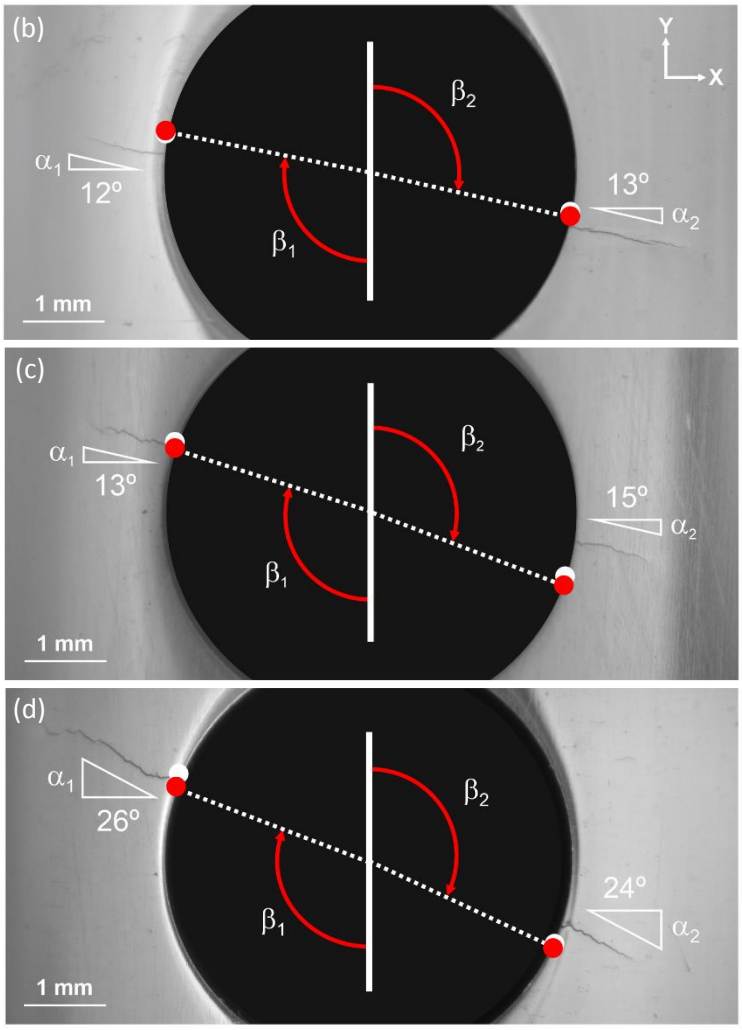

Figure 4. Crack initiation sites and crack angles at the early stage of grow for different loading cases: (a) $\sigma/\tau = 4$; (b) $\sigma/\tau = 2$; and (c) $\sigma/\tau = 4/3$. Red circles and white circles represent the predictions based on the elastic-plastic and the linear-elastic simulations, respectively.

Table 4. Crack initiation sites and directions of crack initiation.

Loading case	1	2	3	4	5	6	7	8
Experimental observations								

β_1 (°)	97.2	94.4	108.6	119.6	99.6	109.6	112.1	105.2
β_2 (°)	104.7	109.6	106.6	92.6	103.7	98.8	109.1	107.1
α_1 (°)	12.2	14.1	17.6	20.3	13.0	13.9	26.2	21.9
α_2 (°)	12.6	13.6	8.1	23.2	15.0	17.5	24.9	25.3
Elastic-plastic predictions								
β_1 (°)	101.2	101.2	101.1	107.5	107.1	106.6	109.7	110.8
β_2 (°)	102.5	102.6	102.8	110.9	111.3	111.9	116.2	114.9
α_1 (°)	11.3	11.3	11.3	18.8	18.8	18.8	22.7	22.7
α_2 (°)	11.3	11.3	11.3	18.9	18.9	18.91	22.8	22.8
Linear-elastic predictions								
β_1 (°)	101.8	101.8	101.8	109.2	109.2	109.2	113.9	113.9
β_2 (°)	100.7	100.7	100.7	107.8	107.8	107.8	113.9	113.9
α_1 (°)	11.8	11.8	11.8	19.2	19.2	19.2	23.9	23.9
α_2 (°)	10.7	10.7	10.7	17.8	17.8	17.8	23.9	23.9

The crack initiation sites were successfully predicted from the nodes with maximum values of the first principal stress which are identified in Figure 4 by the red dots. These results confirm the experimental observations, i.e. an increase of the β angle for higher normal stress to shear stress ratios. The comparison between the experimental observations and the numerical predictions obtained with the cyclic elastic-plastic numerical models is presented in Figure 5. We can see that the data show a good correlation and most of the results have differences lower than 10º. On the average, the errors were equal to 6.1° and 8.3° for the β_1 and β_2 angles, respectively.

For comparison purposes, the predictions computed from the linear-elastic models are also displayed in Figure 4, see the white dots. As can be observed, the differences are not particularly expressive. In this case, the average errors for the β_1 and β_2 angles were equal to 6.3° and 7.4°, respectively. Overall, we can conclude that both models (i.e. elastic-plastic and linear-elastic) led to similar predictive errors, which is an interesting outcome. This is also clear in Figure 5(b) which plots the elastic-plastic predictions against the linear-elastic ones. In fact, the results show a strong correlation, regardless of the loading case, with maximum differences lower than 4º.

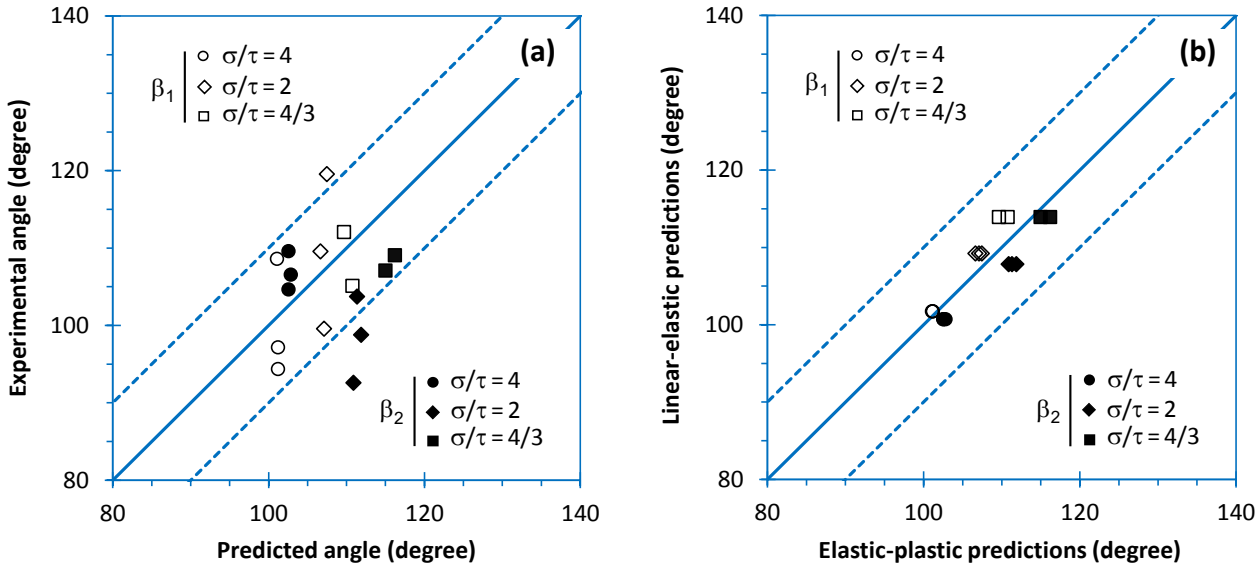

Figure 5. Comparison of crack initiation sites: (a) elastic-plastic predictions versus experimental observations; and (b) elastic-plastic predictions versus linear-elastic predictions.

Another important issue in multiaxial fatigue design is the prediction of crack direction [29-30]. Figure 4 shows examples of the surface crack trajectories observed in the experiments for the tested cases. In this geometry, the crack angles at the early stage of growth are significantly affected by the normal stress to shear stress ratio. In general, it can be stated that the higher the shear stress level, the higher the angle formed by the crack path and the horizontal direction (see α_1 and α_2). It can also be concluded that the angles at both sides of the hole are relatively similar, not varying more than 2°. In some cases, the crack paths exhibited some serration, which may be associated with the manufacturing process.

The numerical predictions computed with the elastic-plastic constitutive model confirmed the above-mentioned observations. In this study, the crack angles at the early stage of growth were determined a priori by computing the first principal direction at the initiation site (i.e. at the node with maximum value of the first principal stress). As can be seen in Figure 6(a), the numerical values agree well with the experimental observations for both sides of the hole. In this case, the predicted angles do not differ more than ±6° from the

experiments. The differences, on average, are relatively small, i.e. 3.2° and 2.6° for α_1 and α_2, respectively. It can also be inferred that the numerical predictions for both sides are similar.

Regarding the effect of the multiaxial loading case on the crack initiation angle, the increase of the normal stress to shear stress ratio, which is associated with a reduction of the mixed-mode level due to a higher contribution of the mode-I loading component, leads to smaller angles. This behaviour agrees with the results available in the literature for thin-walled structures subjected to proportional and non-proportional loading [27-28]. Zerres et al. [27] successfully predicted the crack initiation angle in notched hollow cylindrical geometries subjected to in-phase and out-of-phase histories based on the maximum tangential stress. Luo et al. [28] determined the direction of crack initiation in tubular specimens with circular holes by applying a notch critical plane approach.

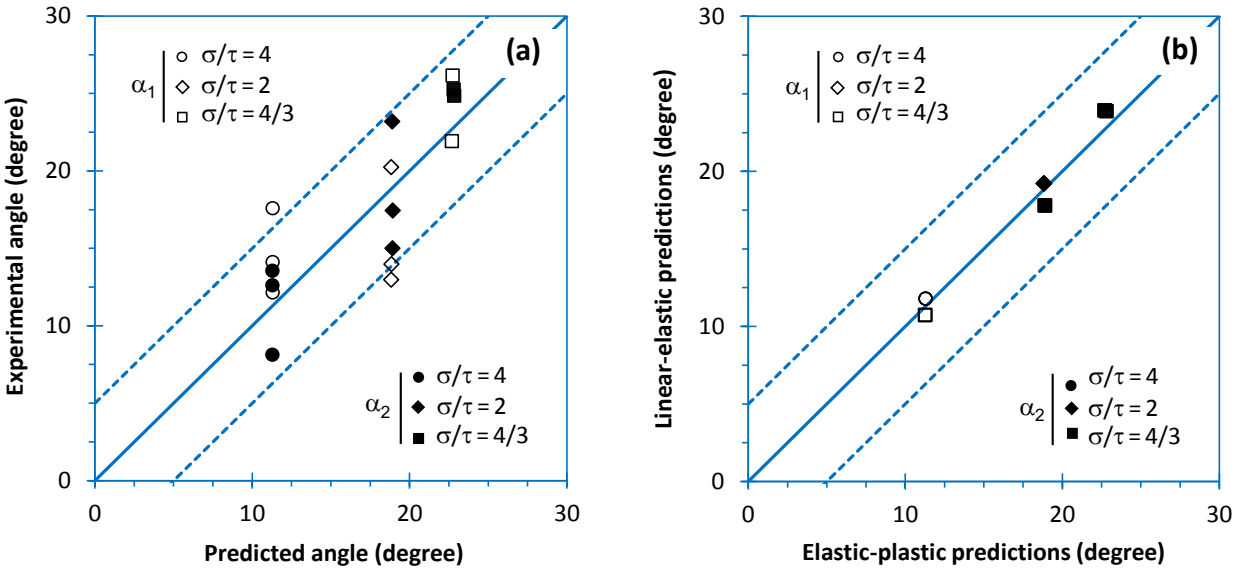

Figure 6. Comparison of crack direction: (a) elastic-plastic predictions versus experimental observations; and (b) elastic-plastic predictions versus linear-elastic predictions.

Similar to the previous case, both the elastic-plastic and the linear-elastic approaches have shown identical predictive capabilities with regard to the direction of crack at the early stage of growth. Figure 6(b) compares the numerical values obtained with the two constitutive models for the studied cases. As can be seen, the results are very-well correlated for the two sides of the hole, irrespective of the normal stress to shear stress ratios, with maximum

differences lower than 1.3º. Note that linear-elastic and elastic-plastic predictions for the same bending-torsion ratio were similar for the different loading levels, see Table 4, which explains the smaller number of data points shown in the figure. This is an interesting conclusion in a practical fatigue design perspective, because the complexity associated with the numerical modelling and the computational time of the two approaches is substantially different, but the final results are similar.

Based on the numerical simulations, it can be hypothesised that the crack initiation sites are located at the wall surface of the hole, near the outer diameter (see Figure 7). Their positions vary with the loading case and tend to move to the inner part, as the normal stress to shear stress ratio decreases. The examination of fracture surfaces by scanning electron microscopy provided support for this reasoning. In fact, the cracks initiated at the wall of the hole (see the dashed lines) from un-melted regions, mainly caused by lack of fusion or inadequate penetration, which has been identified in the literature as the main causes of fatigue crack initiation in maraging steels processed by laser beam powder bed fusion [12,23,31].

Regarding the crack initiation sites, although there is not a perfect match between the predicted ones and the experimental observations, we can see that the results are relatively close. On the other hand, it is reasonably to argue that the defects introduced by the additive manufacturing process strongly changed the stress-strain fields, acting as local stress raisers, and moving the crack initiation site to a different location in the neighbourhood of the predicted point. Figure 7 also compares the crack initiation sites predicted with the elastic-plastic (red arrows) and the linear-elastic (white arrows) models. It is worth to note that the two numerical approaches allow to obtain similar results with no significant differences. In general, the elastic-plastic predictions are shifted slightly to the outer part of the wall.

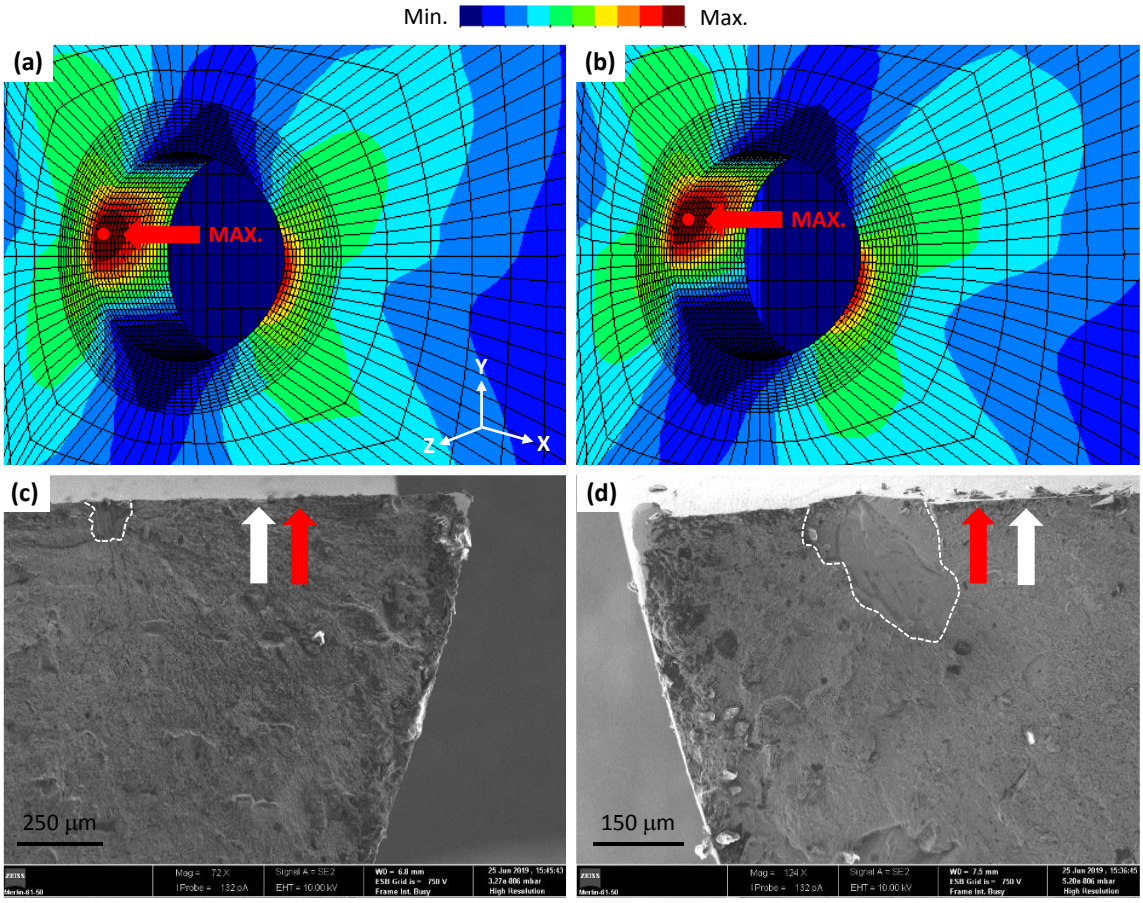

Figure 7. First principal stress fields obtained with the elastic-plastic constitutive models for: (a) $\sigma/\tau = 4$; and (b) $\sigma/\tau = 2$. Scanning electron micrographs of fracture surfaces near the hole surface: (c) $\sigma/\tau = 4$; and (d) $\sigma/\tau = 2$. Red and white arrows represent the crack initiation sites determined from the elastic-plastic and the linear-elastic constitutive models, respectively.

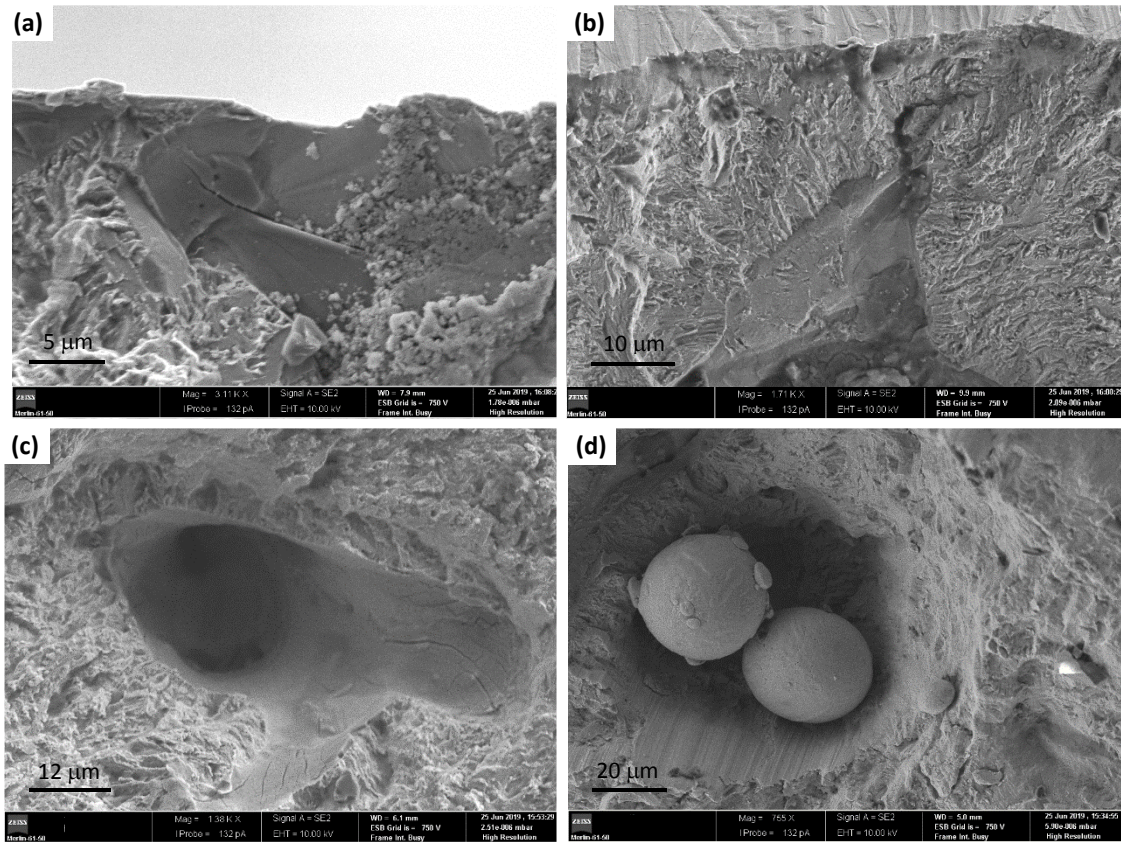

Figure 8. Examples of processing defects found at the fracture surfaces in the SEM analysis: (a) lack of fusion at surface; (b) lack of fusion at sub-surface; (c) internal void; and (d) internal void and un-melted powder particles.

The analysis of SEM micrographs with high magnification, as can be seen in Figure 8, has shown the presence of different types of voids and un-melted powder particles throughout the fracture surfaces. Although the outer surface of the samples has been machined and polished, which significantly reduced the surface roughness and also the notch effect, remnant sub-surface defects, located close the surface, were also found (see Figure 8(a) and Figure 8(b)). These defects may play an important role in the fatigue crack nucleation mechanisms and, naturally, they are also associated with the entire fatigue process.

It is was also concluded from the SEM analysis that the families of voids and un-melted powder particles exist throught the fracture surfaces but have quite different shapes, sizes, and distributions, which is a specificity of the laser beam powder bed fusion process. Despite the inner

defects can affect the fatigue behaviour, defects closer to the outer surface tend to be more detrimental. This is because the crack nucleation is generally associated with the locations of higher cyclic plastic deformation. Thus, surface and sub-surface defects, due to the plane stress state condition, are subjected to more plastic deformation. In addition, since these defects are closer to the surface, they have a greater chance to cause failure, because there is a shorter distance towards an open surface.

4.2. Stress-strain response at the notch region

An accurate evaluation of the stress-strain response at the notch region is fundamental to ensure reliable fatigue life predictions. In this study, as stated in Section 3, the nonlinear finite-element simulations were performed by applying five loading cycles. This number of loading cycles, which was optimised in a previous study [21] focused on a conventional high-strength steel, aimed at attaining a stabilised cyclic stress-strain response of the material. For the conventional high-strength steel, the analysis was carried using the strain energy density and the energy variations between the first and the fifth cycles were lower 0.4% [21].

Figure 9 plots, as an example, the variations of the normal stress range $\Delta\sigma_{YY}$ and the shear stress range $\Delta\tau_{XY}$ at the crack initiation site with the number of applied cycles for the different loading cases. It is clear that $\Delta\sigma_{YY}$ (see Figure 9(a)) and $\Delta\tau_{XY}$ (see Figure 9(b)) do not suffer significant changes during the loading cycles of the numerical simulations and, therefore, the stabilised response is achieved at an early stage. Moreover, as expected, at the same normal stress to shear stress ratio, the higher is the load level, the higher are the local $\Delta\sigma_{YY}$ and the $\Delta\tau_{XY}$ stress components.

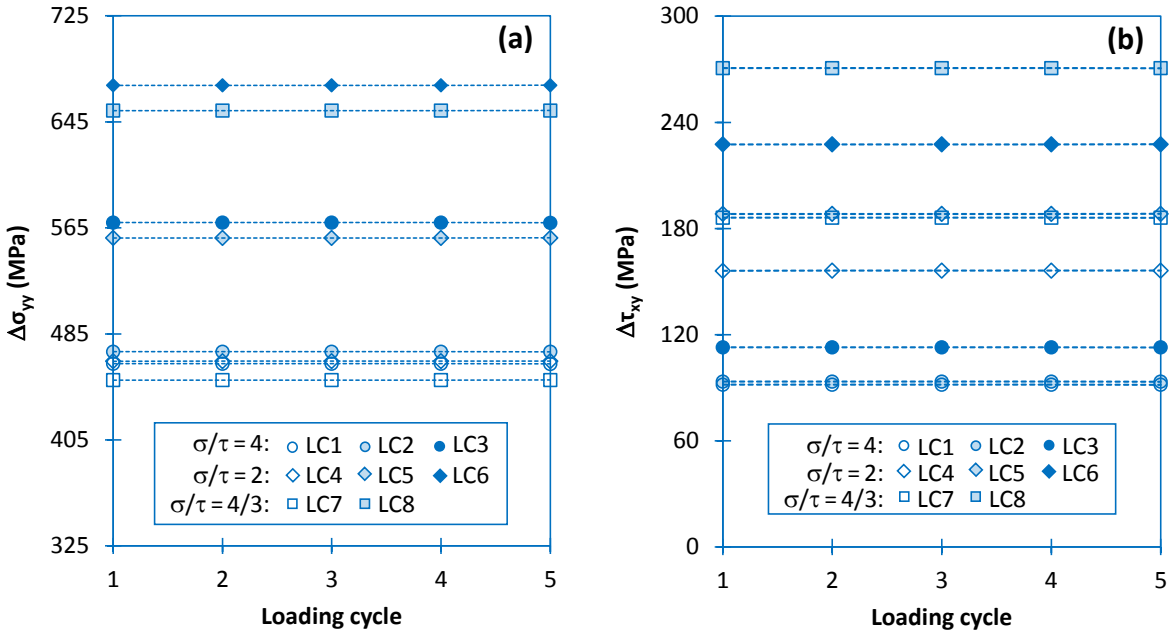

Figure 9. Variation of the: (a) normal stress range $\Delta\sigma_{YY}$ and the (b) shear stress range $\Delta\tau_{XY}$ with the number of cycles at the crack initiation sites for the different loading cases.

Based on the simulations performed for the fifth cycle, which was selected in this study for fatigue assessment, we can characterise the stabilised stress-strain response at the notch region. Figure 10(a) and Figure 10(b) plot the typical profiles of the maximum von Mises stress (σ_{vM}) and the maximum von Mises strain (ε_{vM}) for the peak load along a straight line emanating from the crack initiation site in a direction normal to the hole surface. The stress is maximum at the hole surface and then diminishes progressively to an asymptotic value, where the notch effect is no longer acting. As far as the strain is concerned, the conclusions are basically the same, i.e. the maximum occurs at the surface and then we decrease towards an asymptotic value which depends on the magnitude of the applied loading.

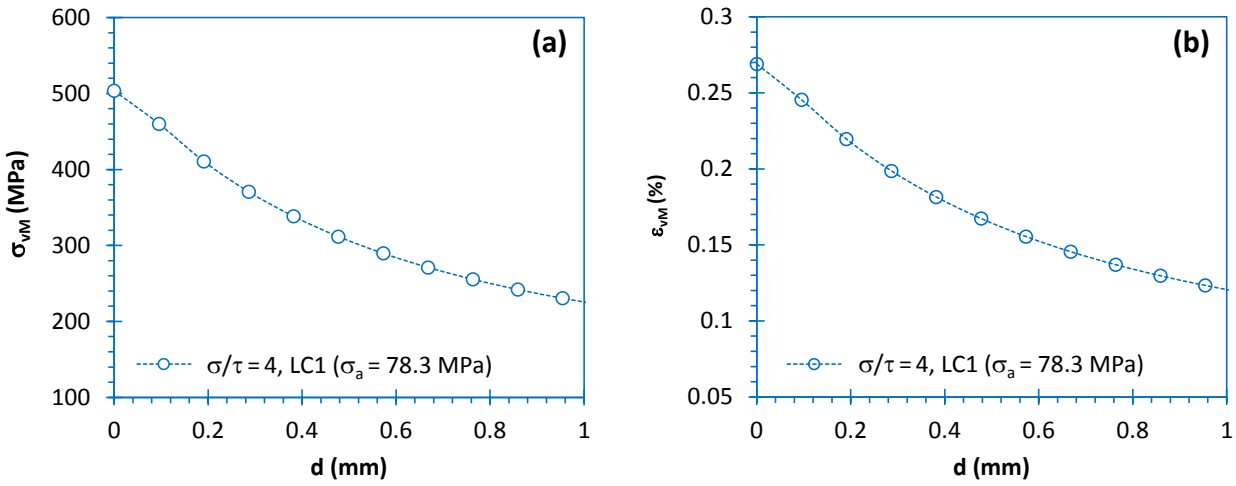

Figure 10. Evolution of (a) von Mises stress and (b) von Mises strain with the distance from the crack initiation site along a straight line normal to the hole surface for the peak load.

In a dimensionless form, the stress and strain profiles are not significantly affected by the loading scenario. For the sake of comparability, several selected cases are displayed in Figure 11(a) and Figure 11(b). The von Mises stress and the von Mises strain were divided by the maximum values; and the distance from the crack initiation site was divided by the material characteristic length (a_0). Overall, the dimensionless functions are overlapped in the entire range, evidencing reduced effect of the loading case. This behaviour has already been reported in previous papers for the dimensionless stress distributions computed with linear-elastic models considering the same loading cases [12].

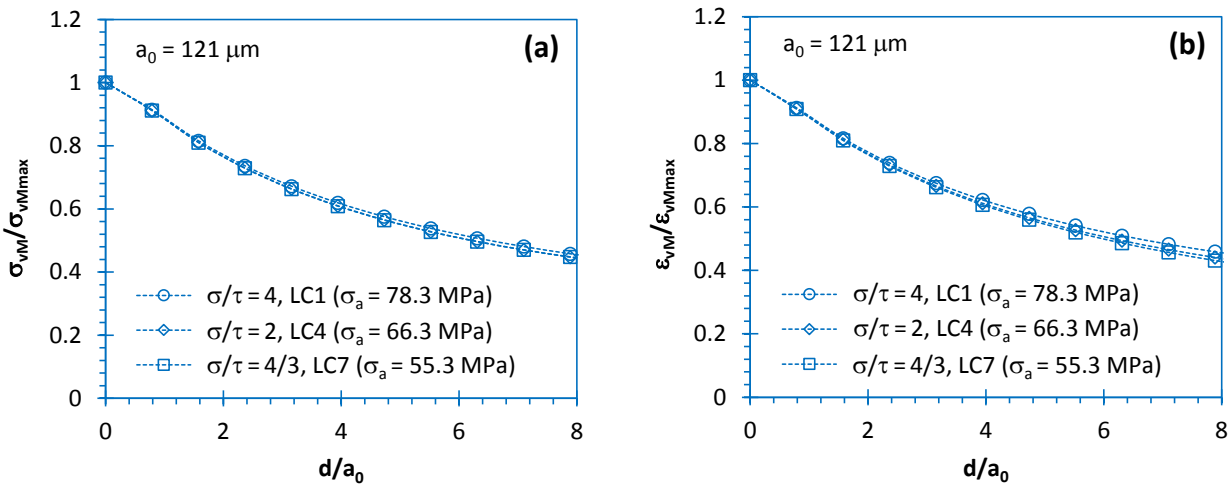

Figure 11. Evolution of (a) dimensionless von Mises stress and (b) dimensionless von Mises strain with the normalised distance from the crack initiation site along a straight line normal to the hole surface for the peak load.

4.3. Fatigue life assessment

The fatigue life assessment was carried out using a model based on the Smith-Watson-Topper (SWT) damage parameter (see Fig. 12). The modus operandi consists of: (1) reduction of the multiaxial stress-strain state to an equivalent uniaxial stress-strain state; (2) calculation of an effective value of the SWT damage parameter at the notch-controlled process zone; and (3) estimation of fatigue lifetime using a SWT-life fatigue master curve [32-33]. Here the model is applied using the elastic-plastic constitutive models. In a previous research conducted by the authors, this concept has been successfully implemented within a linear-elastic framework [12].

The reduction of the multiaxial stress-strain state to an equivalent uniaxial stress-strain state (see Figure 12(a)) was done by computing both the equivalent von Mises stress (σ_{vM}) and the equivalent von Mises strain (ε_{vM}) at the notch region (see Section 4.2). Regarding the effective value of the SWT parameter (see Figure 12(b)), it was computed using the Point Method (PM) of the Theory of Critical Distances (TCD) over a straight line emanating from the crack initiation site along the crack direction at the early stage of growth. Note that the crack initiation site was defined by α, and the direction of crack at the early stage of growth was defined by β. As demonstrated in Section 4.1, the numerical predictions were quite close to the experimental observations.

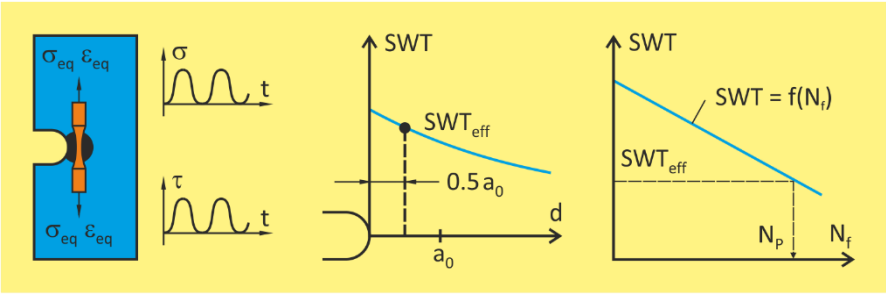

Figure 12. Schematic presentation of the fatigue life prediction model employed in the present study: (a) reduction of multiaxial stress-strain state to an uniaxial equivalent stress-strain state; (b) calculation of an effective value of the SWT damage parameter; and (c) prediction of multiaxial fatigue life using an uniaxial SWT-based fatigue master curve.

Figure 13(a) displays the variation of the SWT damage parameter against the distance from the crack initiation site in natural coordinates for three stress levels and the same normal stress to shear stress ratio ($\sigma/\tau = 2$). At the hole surface, the fatigue damage quantifier is maximum and then reduces progressively towards an asymptotic value. This maximum value is governed by the nominal stress level which affects not only the peak value but also the gradients of the of the SWT damage parameter at the notch-affect zone. Predictably, the peak and the asymptotic values of the SWT damage parameter increase with the increase of the nominal normal stress amplitude (σ_a). The effective values of the SWT damage parameter, represented by the dashed vertical line, are naturally affected by the loading level.

The evolution of the SWT damage parameter with the distance from the crack initiation site in normalised coordinates for the different loading cases studied here is plotted in Figure 13(b). The values of the SWT damage parameter were divided by the maximum value, and the distance from the crack initiation site was divided by the material characteristic length (a_0). In this representation, unlike the previous figure, all functions are perfectly overlapped and follow the same trend. This means that the effective value of the SWT damage parameter occupies a fix position, i.e. approximately 95% of the peak, and that the asymptotic value is also similar for all cases, i.e. near 20% of the maximum value of the dimensionless SWT damage parameter.

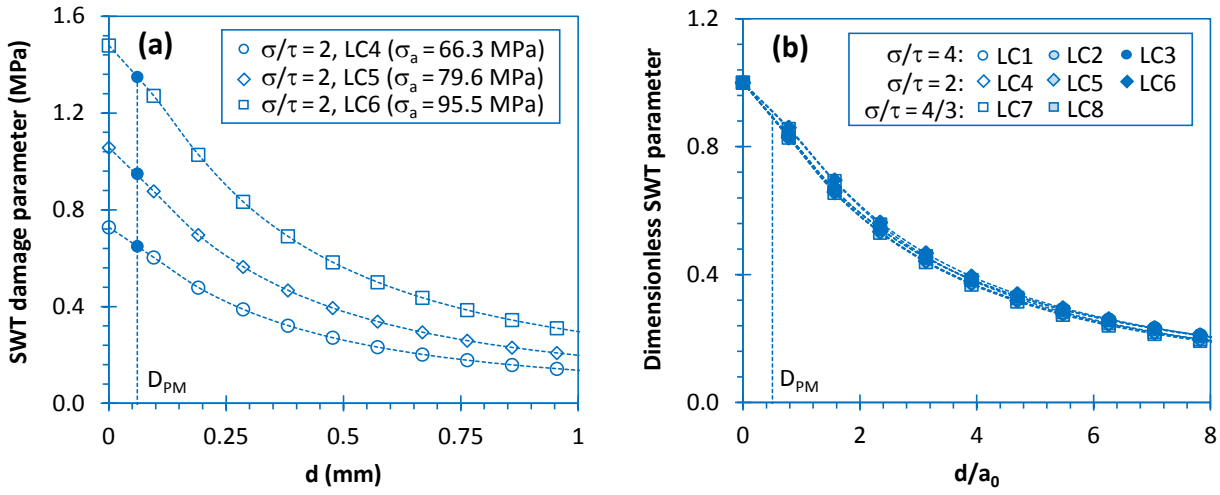

Figure 13. (a) SWT damage parameter against the distance from the crack initiation site; (b) Dimensionless SWT damage parameter against the normalised distance from the crack initiation site for different loading cases over a straight line along the direction of crack at the early stage of growth.

The effective values of the SWT damage parameter (SWT_{eff}) determined for the different loading cases using the above-mentioned procedure are summarised in Table 5. These values were inserted into the uniaxial SWT-based fatigue master curve (see Figure 12(c)) of the tested material to estimate the fatigue crack initiation life. The fatigue master curve of the additively manufactured maraging steel was determined in a previous study (see Eq. (5)) using standard smooth specimens subjected to uniaxial strain-controlled and stress-controlled conditions [12]:

$$\sigma_{max}\varepsilon_a = 10^{1.5315}\left(N_f\right)^{-0.3567} \tag{5}$$

where N_f is the number of cycles to failure. This power function is valid for both the low-cycle and high-cycle fatigue regime for $N_f < 10^6$ cycles.

The fatigue crack initiation life (N_{EP}) calculated for the tested cases from the elastic-plastic simulations is listed in Table 5. Figure 14(a) plots the predicted values against the experimental lives for the different loading cases. For the sake of comparability, scatter bands with factors of

two were plotted. As can be seen, the results are in very good agreement. The errors are relatively small, with only one point outside the scatter bands. Moreover, the predictions are distributed in a balanced way among the conservative and non-conservative regions. Overall, these trends demonstrate the high predictive capabilities of the proposed approach to assess the multiaxial fatigue lifetime in maraging steel produced by laser beam powder bed fusion.

Table 5. Effective values of the SWT damage parameter and fatigue life predictions (Point Method).

Loading case	1	2	3	4	5	6	7	8
SWT_{eff} (MPa)	0.603	0.624	0.911	0.677	0.939	1.452	0.638	1.338
N_i (cycles)	35,115	75,516	20,037	52,883	32,677	7947	84,204	8514
N_{EP} (cycles)	81,156	73,634	25,543	58,767	23,451	6912	69,214	8683
N_{LE} (cycles)	63,054	56,418	20,889	56,087	20,409	7665	54,153	8368

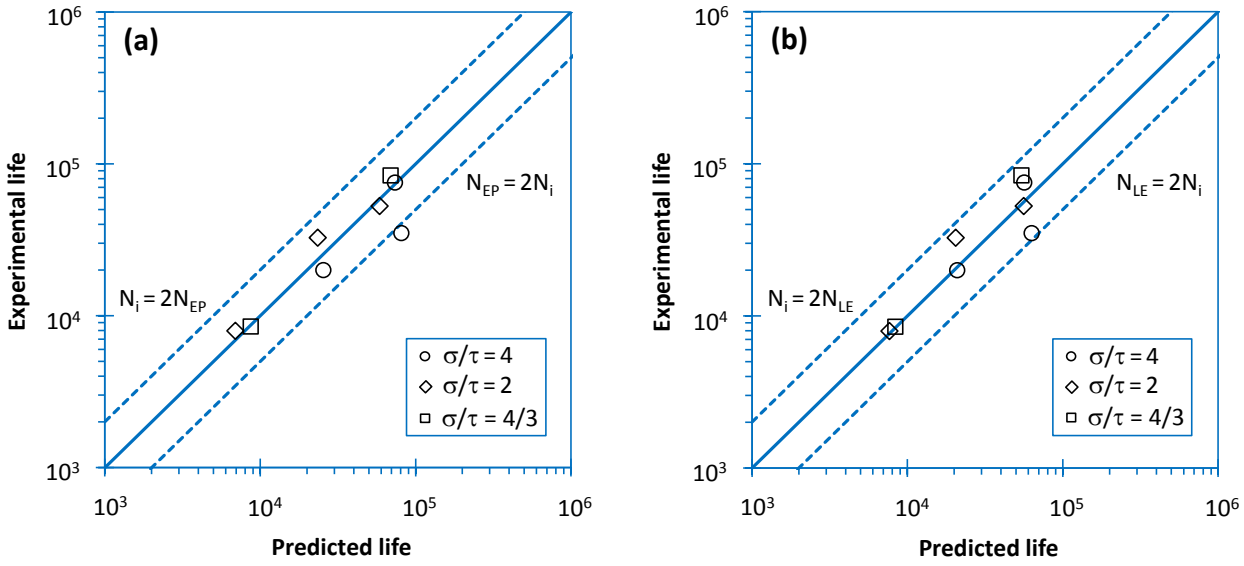

Figure 14. Predicted lives versus experimental lives: (a) elastic-plastic constitutive model; and (b) linear-elastic constitutive model.

The elastic-plastic predictions were compared with those obtained with the linear-elastic simulations. The linear-elastic predictions were done by using the methodology proposed by the authors in a previous paper [12]. Indeed, the methodology is rather similar to that schematised in Figure 12. However, prior to the determination of the effective value of the SWT parameter, the pseudo-elastic energy in the yielded zone is converted into an equivalent elastic-plastic energy using the modified Equivalent Strain Energy Density concept [34]. This energy allows the definition

of a cyclic stress-strain hysteresis loop which is used to determine the effective value of the SWT parameter. Similarly to the elastic-plastic analysis, the Point Method of the Theory of Critical Distances was used. More details about the procedure can be found in reference [12].

The fatigue crack initiation life computed with the linear-elastic models (N_{LE}) for the different loading cases is listed in Table 5. The comparison between the numerical predictions and the experimental lives (N_i) is exhibited in Figure 14(b). For the sake of comparability, scatter bands with factors of two were also plotted. It is worth to note that there is a very good agreement between the numerical and the experimental results. We can see that all points are within the scatter bands and are also balanced among the conservative and non-conservative areas. In addition, it is clear that the predictive capabilities of both approaches are relatively similar, which is an interesting finding.

In order to better evaluate the accuracy of the two tested approaches, a statistical analysis based on the probability density function of the prediction error (P_E) was conducted:

$$P_E = \mathrm{Log}\,(N_i) - \mathrm{Log}\,(N_p) \tag{6}$$

where N_i is the experimental life, and N_p is the predicted life (i.e. N_{EP} or N_{LE}). More accurate models are generally associated with lower standard deviations and mean errors closer to zero. According to Figure 15, the elastic-plastic approach led to mean errors closer to zero but slightly shifted to the non-conservative region, while the linear-elastic gave smaller standard deviations associated with predictions slightly conservative. Nevertheless, as hypothesised above, the two approaches are rather similar. In sum, the results show that both can be used in the fatigue design of maraging steel fabricated by laser beam powder bed fusion subjected to multiaxial loading.

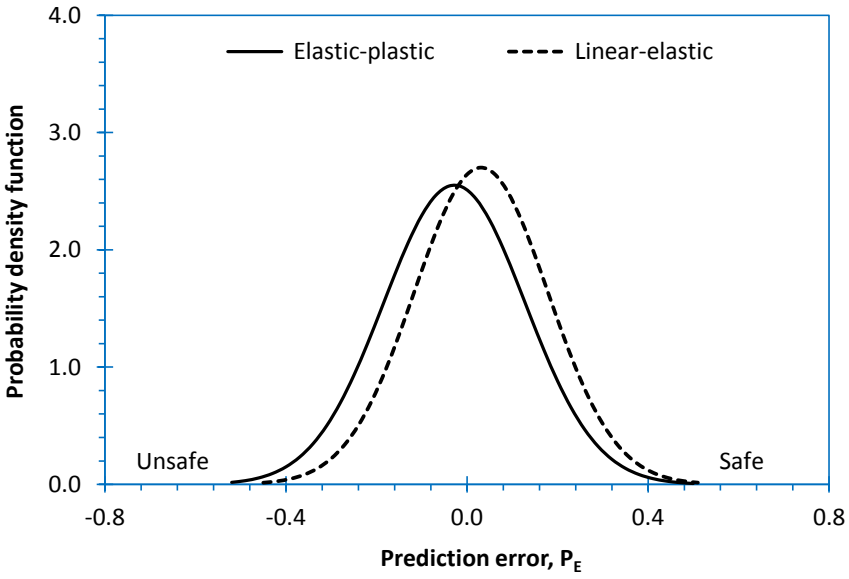

Figure 15. Probability density function of the predictive error for the approaches based on the elastic-plastic and linear-elastic constitutive models.

5. Conclusions

The present paper addressed the notch fatigue behaviour and the lifetime prediction in maraging steel manufactured by laser beam powder bed fusion subjected to proportional bending-torsion loading. Tests were conducted in tubular geometries with lateral holes considering different normal stress to shear stress ratios and multiaxial loading levels. Elastic-plastic and linear-elastic constitutive models were developed to predict the fatigue crack initiation sites, the directions of crack initiation, and the number of cycles to crack initiation. The fatigue crack initiation sites and the directions of crack initiation were determined from the first principal stress field at the hole surface, while the crack initiation life was estimated from a model based on the effective value of the SWT damage parameter evaluated at the notch-controlled process zone in conjunction with the Theory of Critical Distances. The following conclusions can be drawn:

(1) the fatigue behaviour was characterised by the initiation of two diametrically opposite cracks at the hole surface. As the normal stress to shear stress ratio decreased, the cracks tended to be closer to the transversal plane passing through the hole centre;

(2) The direction of crack initiation was governed by the loading scenario. The lower the normal stress to shear stress ratio, the higher was angle formed by the crack and the transversal plane passing through the hole centre;

(3) the crack initiation sites and the directions of crack initiation were similar for both sides of the hole, irrespective of the σ/τ ratios. Such variables were successfully predicted with nearly the same degree of accuracy using the elastic-plastic and the linear-elastic models;

(4) the generalised isotropic plasticity model with mixed isotropic-kinematic hardening demonstrated to be suitable for simulating of the cyclic plastic behaviour of maraging steel manufactured by laser beam powder bed fusion;

(5) the normalised SWT functions computed at the notch-affected process zone over a straight line along the direction of crack initiation were not affected by the loading scenario. This may explain the success of the SWT damage parameter as a robust fatigue quantifier;

(6) the SWT-based model successfully predicted the fatigue crack initiation of additively manufactured maraging steel under bending-torsion. The predictive capabilities of the elastic-plastic and the linear-elastic approaches were similar and close to the experiments.

Acknowledgment

This research is sponsored by FEDER funds through the program COMPETE – Programa Operacional Factores de Competitividade – and by national funds through FCT – Fundação para a Ciência e a Tecnologia –, under the project UIDB/00285/2020.

References

1. Socie D, Marquis G. Multiaxial fatigue. SAE International; 1999. ISBN 978-0768004533
2. Carpinteri A, Spagnoli A, Vantadori S, Viappiani D. A multiaxial criterion for notch high-cycle fatigue using a critical-point method. Eng Fract Mech 2008;75:1864–74. https://doi.org/10.1016/j.engfracmech.2006.11.002.
3. Fatemi A, Molaei R, Phan N. Multiaxial fatigue of additive manufactured metals: Performance, analysis, and applications. Int J Fatigue 2020;134, 105479 https://doi.org/10.1016/j.ijfatigue.2020.105479
4. Sanaei N, Fatemi A (2020). Defects in additive manufactured metals and their effect on fatigue performance: A state-of-the-art review. Prog Mater Sci 2020;117, 100724. https://doi.org/10.1016/j.pmatsci.2020.100724
5. Kempen K, Yasa E, Thijs L, Kruth JP, Van Humbeeck J. Microstructure and mechanical properties of selective laser melted 18Ni-300 steel. In: Physics Procedia; 2011. https://doi.org/10.1016/j.phpro.2011.03.033

6. Kürnsteiner P, Wilms MB, Weisheit A, Barriobero-Vila P, Jägle EA, Raabe D. Massive nanoprecipitation in an Fe-19Ni-xAl maraging steel triggered by the intrinsic heat treatment during laser metal deposition. Acta Mater 2017;129:52-60. https://doi.org/10.1016/j.actamat.2017.02.069
7. Tan C, Zhou K, Ma W, Zhang P, Liu M, Kuang T. Microstructural evolution, nanoprecipitation behavior and mechanical properties of selective laser melted high-performance grade 300 maraging steel. Mater Des 2017; 134:23-34. https://doi.org/10.1016/j.matdes.2017.08.026
8. Jägle EA, Choi PP, Van Humbeeck J, Raabe D. Precipitation and austenite reversion behavior of a maraging steel produced by selective laser melting. J Mater Res 2014;29:2072-2079. https://doi.org/10.1557/jmr.2014.204
9. Fayazfar H, Salarian M, Rogalsky A, et al. A critical review of powder-based additive manufacturing of ferrous alloys: Process parameters, microstructure and mechanical properties. Mater Des. 2018;144:98-128. https://doi.org/10.1016/j.matdes.2018.02.018
10. Bajaj P, Hariharan A, Kini A, Kürnsteiner P, Raabe D, Jägle EA. Steels in additive manufacturing: A review of their microstructure and properties. Mater Sci Eng A. 2020;772: 138633. https://doi.org/10.1016/j.msea.2019.138633
11. Mooney B, Kourousis K. A Review of Factors Affecting the Mechanical Properties of Maraging Steel 300 Fabricated via Laser Powder Bed Fusion. Metals (Basel). 2020;10(9):1273. https://doi.org/ 10.3390/met10091273
12. Branco R, Costa JD, Martins Ferreira JA, Capela C, Antunes FV, Macek W. Multiaxial fatigue behaviour of maraging steel produced by selective laser melting. Mater Des 2021;201: 109469. https://doi.org/10.1016/j.matdes.2021.109469
13. Carpinteri A, Spagnoli A, Vantadori S, Viappiani D. A multiaxial criterion for notch high-cycle fatigue using a critical-point method. Eng Fract Mech 2008;75:1864–74. https://doi.org/10.1016/j.engfracmech.2006.11.002.
14. Liao D, Zhu SP, Correia JA, de Jesus A, Calçada R (2018). Computational framework for multiaxial fatigue life prediction of compressor discs considering notch effects. Eng Fract Mech 2018;202:423-435. https://doi.org/10.1016/j.engfracmech.2018.08.009
15. Lutovinov M, Cerny J, Papuga J. A comparison of methods for calculating notch tip strains and stresses under multiaxial loading. Frat. ed Integrita Strutt. 2016;38:237-243.

16. Liao D, Zhu SP, Correia JAFO, De Jesus AMP, Berto F. Recent advances on notch effects in metal fatigue: A review. Fatigue Fract Eng Mater Struct. 2020;43:637-659. https://doi.org/:10.1111/ffe.13195
17. Mooney B, Agius D, Kourousis KI. Cyclic Plasticity of the As-Built EOS Maraging Steel: Preliminary Experimental and Computational Results. Appl Sci. 2020; 10(4):1232. https://doi.org/10.3390/app10041232
18. Antunes F, Santos L, Capela C, et al. Fatigue crack growth in maraging steel obtained by Selective Laser Melting. Appl Sci. 2019;9(20):4412. https://doi.org/10.3390/app9204412
19. Carpinteri A, Spagnoli A, Vantadori S (2011). Multiaxial fatigue assessment using a simplified critical plane-based criterion. Int J Fatigue 2011;33, 969–976. https://doi.org/10.1016/j.ijfatigue.2011.01.004
20. Goncalves CA, Araujo JA, Mamiya EN. Multiaxial fatigue: a stress based criterion for hard metals. Int J Fatigue 2005;27:177–87. https://doi.org/10.1016/j.crme.2004.09.003
21. Branco R, Prates PA, Costa JD, Borrego LP, Berto F, Kotousov A, Antunes FV (2019). Rapid assessment of multiaxial fatigue lifetime in notched components using an averaged strain energy density approach. Int J Fatigue 2019;124:89-98. https://doi.org/10.1016/j.ijfatigue.2019.02.005
22. McDiarmid DI. A shear stress based critical-plane criterion of multiaxial fatigue failure for design and life prediction. Fatigue Fract Eng Mater Struct, 1194;17:1475-1484 https://doi.org/10.1111/j.1460-2695.1994.tb00789.x
23. Branco R, Costa JDM, Berto F, et al. Low-cycle fatigue behaviour of AISI 18Ni300 maraging steel produced by selective laser melting. Metals (Basel). 2018;8(1):32. https://doi.org/10.3390/met8010032
24. Branco R, Prates PA, Costa JD, Berto F, Kotousov A. New methodology of fatigue life evaluation for multiaxially loaded notched components based on two uniaxial strain-controlled tests. Int J Fatigue 2018;111:308-320. https://doi.org/10.1016/j.ijfatigue.2018.02.027
25. Menezes LF, Teodosiu C. Three-dimensional numerical simulation of the deep drawing process using solid finite elements. J Mater Proc Technol 2000;97:100-106. https://doi.org/10.1016/S0924-0136(99)00345-3

26. Oliveira MC, Alves JL, Menezes LF. Algorithms and strategies for treatment of large deformation frictional contact in the numerical simulation of deep drawing process. Arch Comput Method Eng, 2008;15:113-162. https://doi.org/10.1007/s11831-008-9018-x
27. Zerres P, Bruning J, Vormwald M. Fatigue crack growth behavior of fine-grained steel S460N under proportional and non-proportional loading. Eng Fract Mech. 2010;77:1822-1834. https://doi.org/10.1016/j.engfracmech.2010.02.008
28. Luo P, Yao W, Susmel L, Li P. Prediction of fatigue damage region with the use of the notch critical plane approach for crack initiation and propagation. Int J Fatigue 2020;135:105533. https://doi.org/10.1016/j.ijfatigue.2020.105533
29. Reis L, Li B, Freitas M. Crack initiation and growth path under multiaxial fatigue loading in structural steels. Int J Fatigue 2009;31:1660–8. https://doi.org/10.1016/j.ijfatigue.2009.01.013.
30. Rozumek D, Marciniak Z, Lesiuk G, Correia JAFO, De Jesus AMP. Experimental and numerical investigation of mixed mode I+II and I+III fatigue crack growth in S355J0 steel. Int J Fatigue 2018;113:160-170. https://doi.org/10.1016/j.ijfatigue.2018.04.005
31. Meneghetti G, Rigon D, Gennari C. An analysis of defects influence on axial fatigue strength of maraging steel specimens produced by additive manufacturing. Int J Fatigue. 2019;118:54-64. https://doi.org/:10.1016/j.ijfatigue.2018.08.034
32. Correia J, Apetre N, Arcari A, et al. Generalized probabilistic model allowing for various fatigue damage variables. Int J Fatigue 2017;100:187-194. https://doi.org/10.1016/j.ijfatigue.2017.03.031
33. Cruces AS, Lopez-Crespo P, Bressan S, Itoh T, Moreno B. On the Behaviour of 316 and 304 Stainless Steel under Multiaxial Fatigue Loading: Application of the Critical Plane Approach. Metals 2019;9:978 https://doi.org/10.3390/met9090978
34. Ye DY, Matsuoka S, Suzuki N, Maeda Y. Further investigation of Neuber's rule and the equivalent strain energy density (ESED) method. Int J Fatigue 2004;26:447-455. https://doi.org/10.1016/j.ijfatigue.2003.10.002

Declaration of interests

☒ The authors declare that they have no known competing financial interests or personal relationships that could have appeared to influence the work reported in this paper.

☒The authors declare the following financial interests/personal relationships which may be considered as potential competing interests:

Notch fatigue analysis and crack initiation life estimation of maraging steel fabricated by laser beam powder bed fusion under multiaixal loading

R. Branco[a], P.A. Prates[a], J.D. Costa[a], J.A. Martins Ferreira[a], C. Capela[b,a], F. Berto[c]

[a] University of Coimbra, CEMMPRE, Department of Mechanical Engineering, Coimbra, Portugal

[b] ESTG, Department of Mechanical Engineering, Instituto Politécnico de Leiria, Leiria, Portugal

[c] Department of Mechanical and Industrial Engineering, NTNU, 7491 Trondheim, Norway

Notch fatigue analysis and crack initiation life estimation of maraging steel fabricated by laser beam powder bed fusion under multiaixal loading

R. Branco[a,1], P.A. Prates[a], J.D. Costa[a], J.A. Martins Ferreira[a], C. Capela[b,a], F. Berto[c]

[a] University of Coimbra, CEMMPRE, Department of Mechanical Engineering, Coimbra, Portugal
[b] ESTG, Department of Mechanical Engineering, Instituto Politécnico de Leiria, Leiria, Portugal
[c] Department of Mechanical and Industrial Engineering, NTNU, 7491 Trondheim, Norway

Abstract

This paper deals with the notch fatigue behaviour and crack initiation life estimation in maraging steel fabricated by laser beam powder bed fusion under multiaxial loading. Tests are conducted in tubular geometries with lateral holes considering different normal stress to shear stress ratios and multiaxial loading levels. The cyclic stress-strain response at the notch-controlled process zone is simulated numerically using two alternative approaches: a generalised isotropic plasticity model with mixed isotropic-kinematic hardening, and a simple linear-elastic model. Both approaches demonstrated to be suitable for predicting the crack initiation sites, the directions of crack growth, and the fatigue life. Fatigue life was calculated from a SWT-based model combined with the Theory of Critical Distances. Elastic-plastic predictions led to smaller errors but slightly shifted to the non-conservative side.

Keywords: multiaxial fatigue, crack initiation, crack direction, cyclic plasticity, SWT damage parameter; maraging steel, powder bed fusion

1. Introduction

The development of reliable models for multiaxial fatigue life assessment is a complex task because, in general, there is a huge number of variables involved in the analysis [1-2]. The paradigm of additive manufacturing become this task more challenging and difficult once this new class of materials is more prone to fatigue failure [3-4]. Within the current additive manufacturing

[1] Corresponding author: R. Branco (ricardo.branco@dem.uc.pt)

processes, laser beam powder bend fusion is one of the most popular techniques. This process combines unique features with cost effectiveness, allowing the fabrication of functional parts in a layer-by-layer fashion directly from three-dimensional digital files. It is currently used in a number of high-value added industries, such as aeronautical, biomedical, automotive and moulds, among others [5-6].

Due to its martensitic matrix which requires a rapid quench from the austenitic region to temperatures below the martensitic start temperature, maraging steel is particularly suited for laser beam powder bed fusion, in particular for selective laser melting [7-8]. There are at least three reasons that may contribute to this success: (1) the small size of the melt pool and the associated high cooling rates; (2) the cyclic reheating during the printing process that may lead to the nucleation of hardening precipitates without heat treatments; and (3) the complex shapes and the limited number of parts required in the typical areas of application. One of the main drawbacks is its susceptibility to different types of anomalies (e.g. porosities, inclusions, lack of fusion, etc.) which may increase the uncertainty concerning the mechanical behaviour.

In the past few years, some effort has been put on the understanding of the mechanical behaviour, particularly on the triangular relationship between process parameters, microstructural features, and mechanical properties [9-11]. Although the research focused on monotonic and cyclic properties is relatively abundant, studies dealing with multiaxial fatigue of maraging steel fabricated by laser powder bed fusion are more limited [12]. A non-trivial problem in multiaxial fatigue is concerned with the accurate prediction of notch behaviour [13]. It requires not only the knowledge about the crack initiation sites and direction of crack growth, but also an accurate evaluation of cyclic plasticity at the geometric discontinuities [14].

Current strategies to deal with the cyclic plasticity response at the geometric discontinuities are usually materialised by means of experimental techniques, numerical methods, or approximate solutions [15]. Experimental techniques, due to their intrinsic nature, have some limitations, such as the difficulty to assess complicated geometric details or the impossibility to analyse the stress-strain fields inside the body [16]. On the other hand, with the advent of computer technology, numerical methods can provide precise results even for complex details, provided that an

adequate constitutive model is implemented. Nevertheless, constitutive relationships for additively manufactured maraging steel have only been derived for uniaxial loading [17-18].

Regarding the multiaxial fatigue life prediction, different models can be used. Within the most successful approaches, we can mention those that reduce the multiaxial stress-stress state to an equivalent uniaxial state [19-22]. In general, this link is formalised through a representative fatigue damage parameter, which can be expressed in terms of stress-based, strain-based, or energy-based relationships. The comparison between the equivalent fatigue damage quantifier and the uniaxial fatigue response allows to define the associated fatigue lifetime. Therefore, in order to develop reliable models for multiaxial fatigue life assessment of maraging steels fabricated by laser beam powder bed fusion, it is necessary to identify representative fatigue damage quantifiers.

This paper aims to address the above-mentioned gaps. Firstly we conduct a series of experimental tests in tubular geometries with lateral holes fabricated by laser beam powder bed fusion subjected to proportional bending-torsion loading. Then, it is implemented a generalised isotropic plasticity model with mixed isotropic-kinematic hardening to simulate the cyclic stress-strain response at the notch-affected zone. A uniaxial equivalent model formulated using a SWT-based quantifier is successfully developed to assess the fatigue lifetime. After that, numerical predictions of fatigue crack initiation, direction of fatigue crack initiation, and fatigue lifetime are compared to those obtained experimentally, and with those obtained with a simple linear-elastic model.

2. Experimental procedure

The specimen geometry used in the multiaxial fatigue tests, which consists of a 3mm-thick tubular configuration with a length of 150 mm and an outer diameter of 16 mm, is presented in Figure 1. It was fabricated vertically, from 18Ni300 maraging steel, using a Concept Laser M3 linear printing system equipped with a 400W Nd:YAG fibre laser. Each layer was created with a constant thickness of 40 μm, a scan speed of 200 mm/s, and a hatch spacing of 100 μm. The average surface roughness of the as-built samples was equal to 12 μm. After the additive manufacturing process, the 5mm-diameter hole was drilled by CNC, and the ~~external~~ outer surface of the samples was machined and polished to a scratch-free condition. The final surface roughness of the outer surface was 0.5 μm. The main mechanical properties are listed in Table 1.

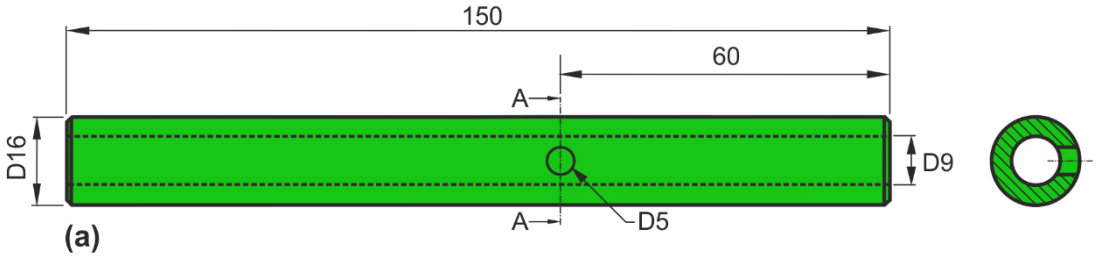

Figure 1. Specimen geometry of additively used in the multiaxial fatigue tests (units: mm).

The bending-torsion tests were performed under in-phase constant-amplitude loading in a conventional servo-hydraulic machine connected to a custom-made gripping system with a stress ratio (R) equal to 0. Three normal stress to shear stress ratios (σ/τ) were considered, namely σ/τ = 4, σ/τ = 2, and σ/τ = 4/3. The nominal normal stresses applied in the notched region are listed in Table 2. The notch region was monitored in situ to detect the crack initiation sites and to track the crack paths along the external surface of the specimen. The crack initiation lives, listed in Table 2, were calculated in a previous paper published by the authors [12] for a crack size equal to the fatigue characteristic length (a_0) defined from the El-Haddad parameter. Under pulsating loading conditions, a_0 = 121 μm [12].

Table 1. Mechanical properties of the additively manufactured 18Ni300 maraging steel.

Property	Value
Porosity (%)	0.74±0.09
Density (g/m^3)	7.42
Hardness (HV1)	354±5
Tensile strength (MPa)	1147±13
Yield strength (MPa)	910±11
Strain at failure (%)	5.12±0.001
Fatigue limit stress range, $\Delta\sigma_0$ (MPa)	266
Stress intensity factor range threshold, ΔK_{th0} (MPa·m$^{0.5}$)	5.2
Cyclic hardening coefficient, K' (MPa)	1921.2
Cyclic hardening exponent, n'	0.110

Table 2. Summary of multiaxial fatigue tests.

Loading case	1	2	3	4	5	6	7	8
σ/τ	4	4	4	2	2	2	4/3	4/3
σ_a (MPa)	78.3	79.6	95.5	66.3	79.6	95.5	55.3	79.6
σ_m (MPa)	86.1	87.6	105.1	73.0	87.6	105.1	60.8	87.6
N_i (cycles)	35,115	75,516	20,037	52,883	32,677	7947	84,204	8514

3. Numerical modelling

In this study, two constitutive models were developed: a linear-elastic, and an elastic-plastic. The former was modelled by the generalised Hooke's law, assuming a continuous, homogeneous, and isotropic behaviour. Regarding the latter, the elastic regime was also modelled via the generalised Hooke's law and the plastic regime was modelled by the von Mises yield criterion coupled with a mixed isotropic-kinematic hardening law under an associated flow rule, as follows:

$$\mathrm{f}(\sigma' - \mathrm{X}) - \mathrm{Y} \leq 0 \qquad (1)$$

where $\mathrm{f}(\sigma' - \mathrm{X})$ represents the von Mises yield criterion, σ' is the deviatoric Cauchy stress tensor, X is the backstress tensor (described by the kinematic hardening law) and Y is the yield stress (described by the isotropic hardening law). For the maraging steel manufactured by laser beam powder bed fusion, Y was modelled using a Voce isotropic hardening law, i.e.

$$\mathrm{Y} = \mathrm{Y}_0 + (\mathrm{Y}_{\mathrm{sat}} - \mathrm{Y}_0)[1 - \exp(-\mathrm{C}_{\mathrm{Y}}\bar{\varepsilon}^{\mathrm{p}})] \qquad (2)$$

where Y_0, $\mathrm{Y}_{\mathrm{sat}}$, and C_{Y} are material parameters and $\bar{\varepsilon}^{\mathrm{p}}$ is the equivalent plastic strain. The same hardening law was used to model the material behaviour of the conventional 34CrNiMo6 high-strength steel used in the gripping system, which was included in the numerical model to simulate as close as possible the experimental tests.

The non-linear kinematic hardening of both materials was modelled by means of an Armstrong-Frederick law:

$$\dot{\mathrm{X}} = \mathrm{C}_{\mathrm{X}}\left[\frac{\mathrm{X}_{\mathrm{sat}}}{\bar{\sigma}}(\sigma' - \mathrm{X}) - \mathrm{X}\right]\dot{\bar{\varepsilon}}^{\mathrm{p}} \qquad (3)$$

where $\dot{\mathrm{X}}$ is the backstress rate, C_{X}, and $\mathrm{X}_{\mathrm{sat}}$ are material parameters, $\bar{\sigma}$ is the equivalent stress, and $\dot{\bar{\varepsilon}}^{\mathrm{p}}$ is the equivalent plastic strain rate. The determination of the material

constants that best described the cyclic elastic-plastic behaviour of both steels was carried out by minimising the function:

$$F(A) = \sum_{i=1}^{N} \left(\frac{\sigma^{Num}(A) - \sigma^{Exp}}{\sigma^{Exp}} \right)_i^2 \quad (4\cancel{6})$$

where $\sigma^{Num}(A)$ and σ^{Exp} are the analytical fitted and the experimentally measured values of true stress at point i (which corresponds to a given equivalent plastic strain value), N is the total number of experimental data points, and A is the set of material parameters to be identified.

The fitting procedure for the additively manufactured 18Ni300 maraging steel was carried out using stress-strain data collected in a low-cycle fatigue test performed under strain-controlled conditions with a strain amplitude ($\Delta\varepsilon/2$) of ±0.8% [23]. The material constants were determined using 6600 points which correspond to the first 33 cycles, i.e. 80% of the total life. Figure 2(a) compares the simulated cyclic stress-strain response with the hysteresis loops at the mid-life cycle. Overall, there is an excellent correlation between the numerical and the experimental results which is an excellent outcome. In relation to the 34CrNiM6 high-strength steel, the fitting process has been successfully done in a previous study for a strain amplitude of ±2.0% (see Figure 2(b)) and the numerical results are very good agreement with the experimental data [24]. The fitted constants for both materials are summarised in Table 3.

Table 2. Fitted elastic-plastic parameters for the simulated materials.

Material	Hooke law		Voce law		Armstrong-Frederick law		
	E (GPa)	ν	Y_0 (MPa)	Y_{sat} (MPa)	C_Y	Cx	X_{sat} (MPa)
18Ni300	168.0	0.330	683.62	683.62	0	728.34	402.06
34CrNiMo6	209.8	0.296	741.51	741.51	0	87.60	212.16

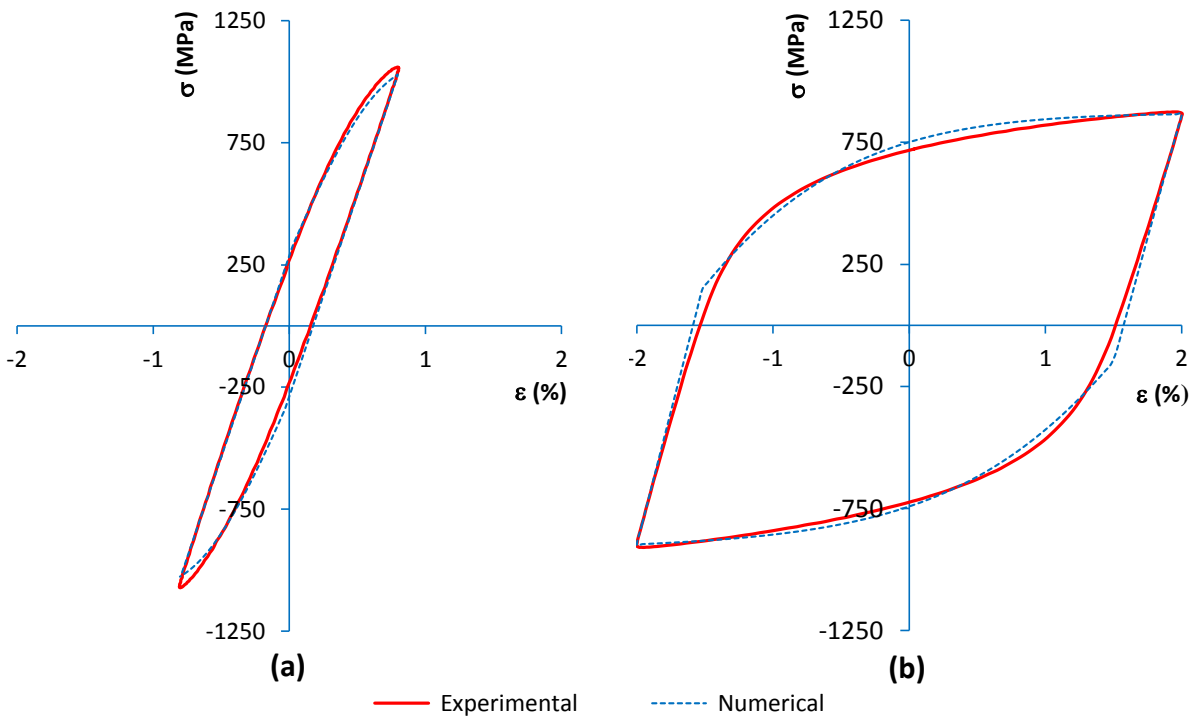

Figure 2. Simulated and experimental stress-strain hysteresis loops for the: (a) additively manufactured 18Ni300 maraging steel manufactured at $\Delta\varepsilon/2 = \pm 0.8\%$; and (b) conventional 34CrNiMo6 high-strength steel at $\Delta\varepsilon/2 = \pm 2.0\%$. Experimental cycles refer to the hysteresis loop collected at the mid-life.

Figure 3 shows the finite element model used in this study. As can be seen, it includes the specimen geometry, represented in green, and a prismatic bar, part of the gripping system, connected to the end of the specimen, represented in purple. The material of the specimen was modelled using the material constants of the additively manufactured 18Ni300 maraging steel, and the material of the prismatic bar was modelled using the material constants of the conventional 34CrNiMo6 high-strength steel. DD3Imp, an implicit three-dimensional finite element code developed at the University of Coimbra, was used to perform the numerical simulations [25-26].

The mesh was created in a parametric framework with 8-node isoparametric brick elements, and its density resulted from a trade-off between computational overhead and accuracy. At the geometric discontinuity, an ultrafine mesh was created to evaluate the higher stress-strain gradients that are expected to occur in that region. On the contrary, in the regions further from

the hole, the element size was increased to reduce the simulation time. The assembled model had 152,248 elements and 163,138 nodes, while the refined region around the hole contained 43,000 elements and 48,000 nodes, respectively.

In order to replicate as close as possible the experimental tests, the normal stress to shear stress ratio acting on the notch region was generated from a single force, F, applied on the external prismatic bar connected to the specimen. The outer surface of the other end was fixed for an extension of 30 mm. The magnitude of the force (F) and its point of application (h) were defined in a case-by-case basis. In all simulations, L was fixed. The loading was applied during five cycles, comprising both loading and unloading events, to obtain a stabilised cyclic elastic-plastic response. The stress and strain fields of the last cycle were used in the fatigue analysis.

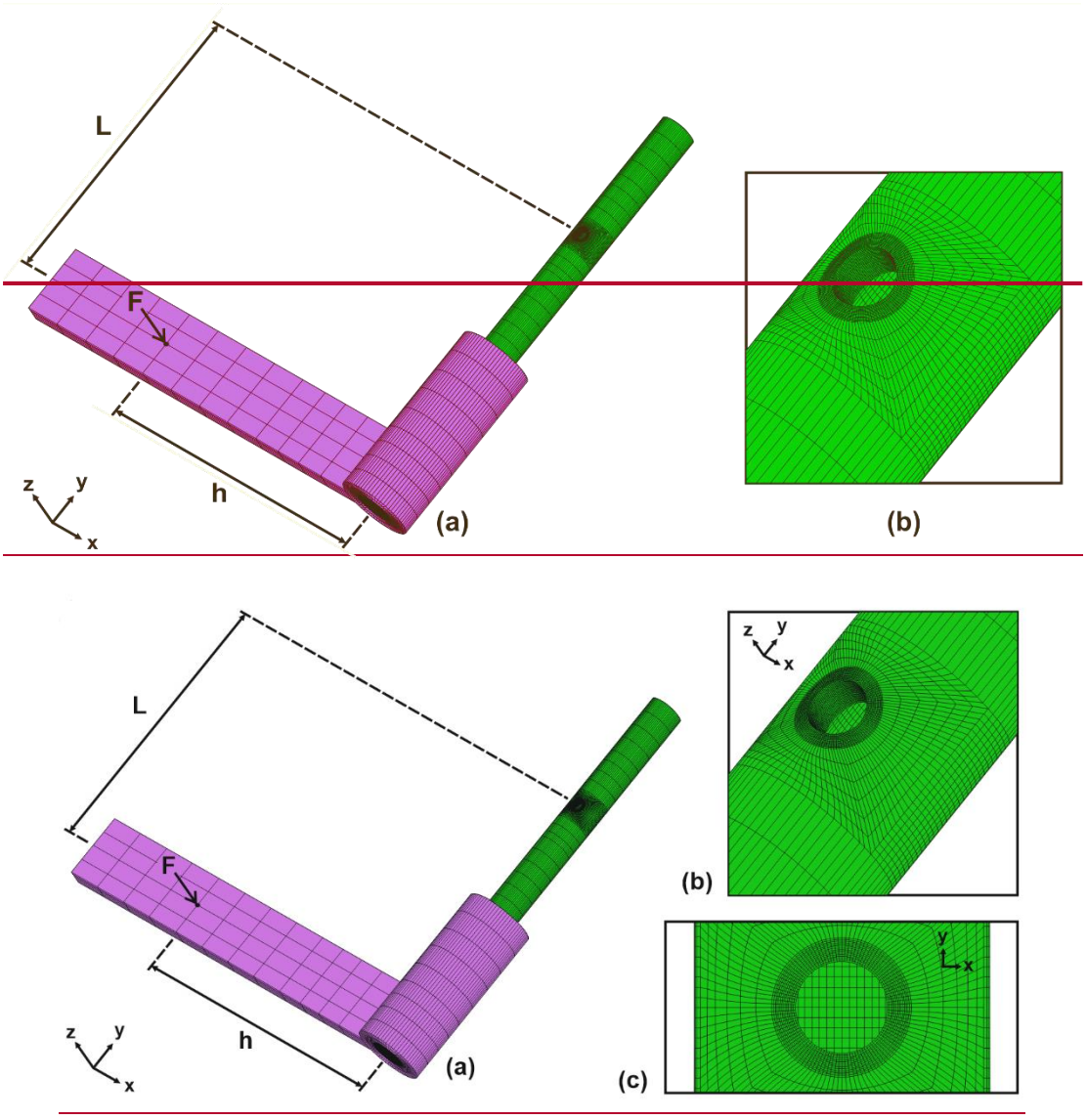

Figure 3. Finite element model used in the linear-elastic and elastic-plastic numerical simulations: (a) assembled model; and (b,c) details of the notch region (green: additively manufactured maraging steel; purple: conventional high-strength steel).

4. Results and discussion

4.1 Notch fatigue behaviour

The notch fatigue behaviour was governed by the normal stress to shear stress ratio (σ/τ). Figure 4 exhibits the typical fatigue crack initiation sites and the fatigue crack angles observed in the experiments at the outer surface of the specimen. The measured values and

the numerical predictions are summarised in Table 4. Regardless of the loading case, two cracks have initiated in diametrically opposite points of the hole. These locations tend to be closer to the longitudinal central plane, represented by the thicker white line, as the σ/τ ratio decreases. Lower σ/τ ratios increase the shear stress level leading to higher degrees of mixed mode loading. Such behaviour is in line with that reported in the literature for thin-walled geometries subjected to multiaxial loading [27-28].

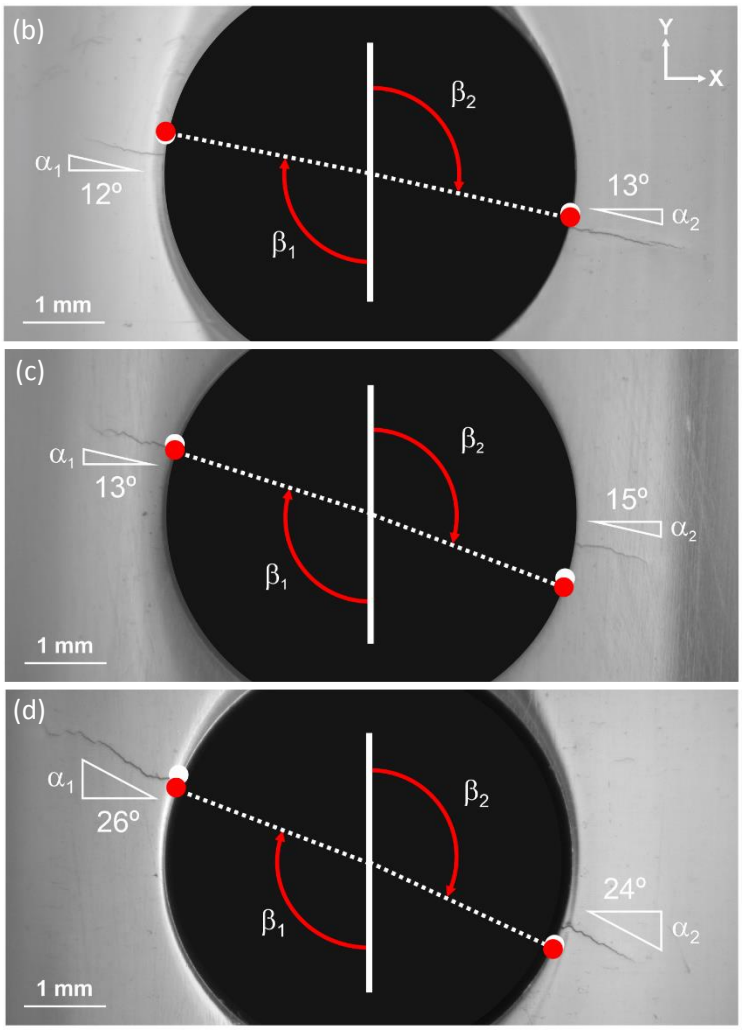

Figure 4. Crack initiation sites and crack angles at the early stage of grow for different loading cases: (a) $\sigma/\tau = 4$; (b) $\sigma/\tau = 2$; and (c) $\sigma/\tau = 4/3$. Red circles and white circles represent the predictions based on the elastic-plastic and the linear-elastic simulations, respectively.

Table 4. Crack initiation sites and directions of crack initiation.

Loading case	1	2	3	4	5	6	7	8
Experimental observations								
β_1 (°)	97.2	94.4	108.6	119.6	99.6	109.6	112.1	105.2
β_2 (°)	104.7	109.6	106.6	92.6	103.7	98.8	109.1	107.1
α_1 (°)	12.2	14.1	17.6	20.3	13.0	13.9	26.2	21.9
α_2 (°)	12.6	13.6	8.1	23.2	15.0	17.5	24.9	25.3
Elastic-plastic predictions								
β_1 (°)	101.2	101.2	101.1	107.5	107.1	106.6	109.7	110.8
β_2 (°)	102.5	102.6	102.8	110.9	111.3	111.9	116.2	114.9
α_1 (°)	11.3	11.3	11.3	18.8	18.8	18.8	22.7	22.7
α_2 (°)	11.3	11.3	11.3	18.9	18.9	18.91	22.8	22.8
Linear-elastic predictions								
β_1 (°)	101.8	101.8	101.8	109.2	109.2	109.2	113.9	113.9
β_2 (°)	100.7	100.7	100.7	107.8	107.8	107.8	113.9	113.9
α_1 (°)	11.8	11.8	11.8	19.2	19.2	19.2	23.9	23.9
α_2 (°)	10.7	10.7	10.7	17.8	17.8	17.8	23.9	23.9

The crack initiation sites were successfully predicted from the nodes with maximum values of the first principal stress which are identified in Figure 4 by the red dots. These results confirm the experimental observations, i.e. an increase of the β angle for higher normal stress to shear stress ratios. The comparison between the experimental observations and the numerical predictions obtained with the cyclic elastic-plastic numerical models is presented in Figure 5. We can see that the data show a good correlation and most of the results have differences lower than 10º. On the average, the errors were equal to 6.1° and 8.3° for the β_1 and β_2 angles, respectively.

For comparison purposes, the predictions computed from the linear-elastic models are also displayed in Figure 4, see the white dots. As can be observed, the differences are not particularly expressive. In this case, the average errors for the β_1 and β_2 angles were equal to 6.3° and 7.4°, respectively. Overall, we can conclude that both models (i.e. elastic-plastic and linear-elastic) led to similar predictive errors, which is an interesting outcome. This is also clear in Figure 5(b) which plots the elastic-plastic predictions against the linear-elastic ones. In fact, the results show a strong correlation, regardless of the loading case, with maximum differences lower than 4º.

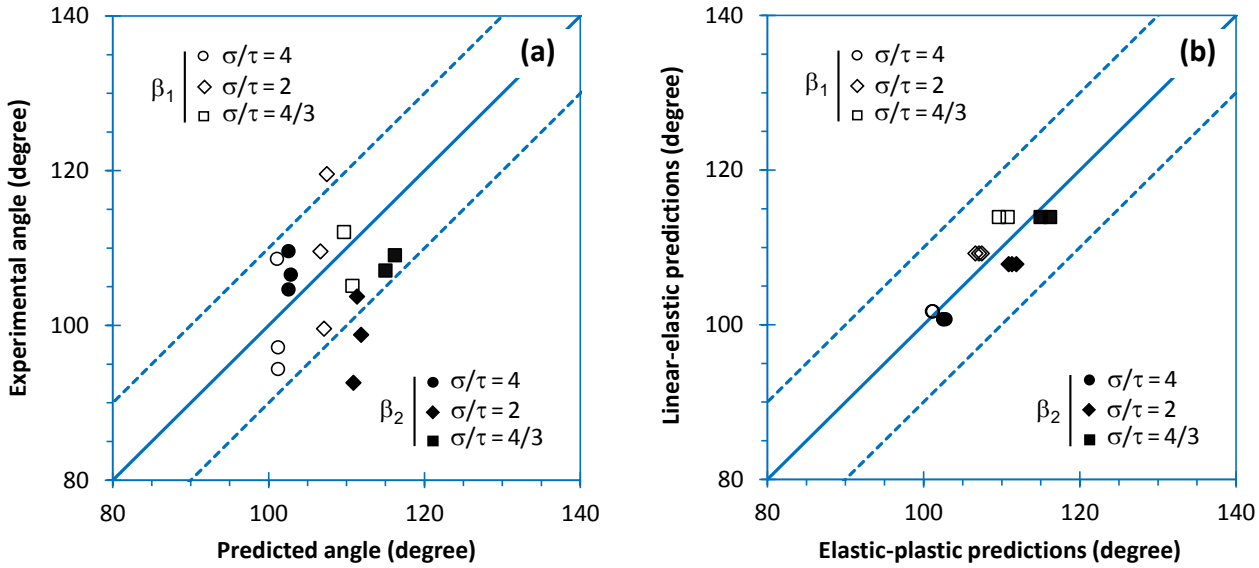

Figure 5. Comparison of crack initiation sites: (a) elastic-plastic predictions versus experimental observations; and (b) elastic-plastic predictions versus linear-elastic predictions.

Another important issue in multiaxial fatigue design is the prediction of crack direction [29-30]. Figure 4 shows examples of the surface crack trajectories observed in the experiments for the tested cases. In this geometry, the crack angles at the early stage of growth are significantly affected by the normal stress to shear stress ratio. In general, it can be stated that the higher the shear stress level, the higher the angle formed by the crack path and the horizontal direction (see α_1 and α_2). It can also be concluded that the angles at both sides of the hole are relatively similar, not varying more than 2°. In some cases, the crack paths exhibited some serration, which may be associated with the manufacturing process.

The numerical predictions computed with the elastic-plastic constitutive model confirmed the above-mentioned observations. In this study, the crack angles at the early stage of growth were determined a priori by computing the first principal direction at the initiation site (i.e. at the node with maximum value of the first principal stress). As can be seen in Figure 6(a), the numerical values agree well with the experimental observations for both sides of the hole. In this case, the predicted angles do not differ more than ±6° from the

experiments. The differences, on average, are relatively small, i.e. 3.2° and 2.6° for α_1 and α_2, respectively. It can also be inferred that the numerical predictions for both sides are similar.

Regarding the effect of the multiaxial loading case on the crack initiation angle, the increase of the normal stress to shear stress ratio, which is associated with a reduction of the mixed-mode level due to a higher contribution of the mode-I loading component, leads to smaller angles. This behaviour agrees with the results available in the literature for thin-walled structures subjected to proportional and non-proportional loading [27-28]. Zerres et al. [27] successfully predicted the crack initiation angle in notched hollow cylindrical geometries subjected to in-phase and out-of-phase histories based on the maximum tangential stress. Luo et al. [28] determined the direction of crack initiation in tubular specimens with circular holes by applying a notch critical plane approach.

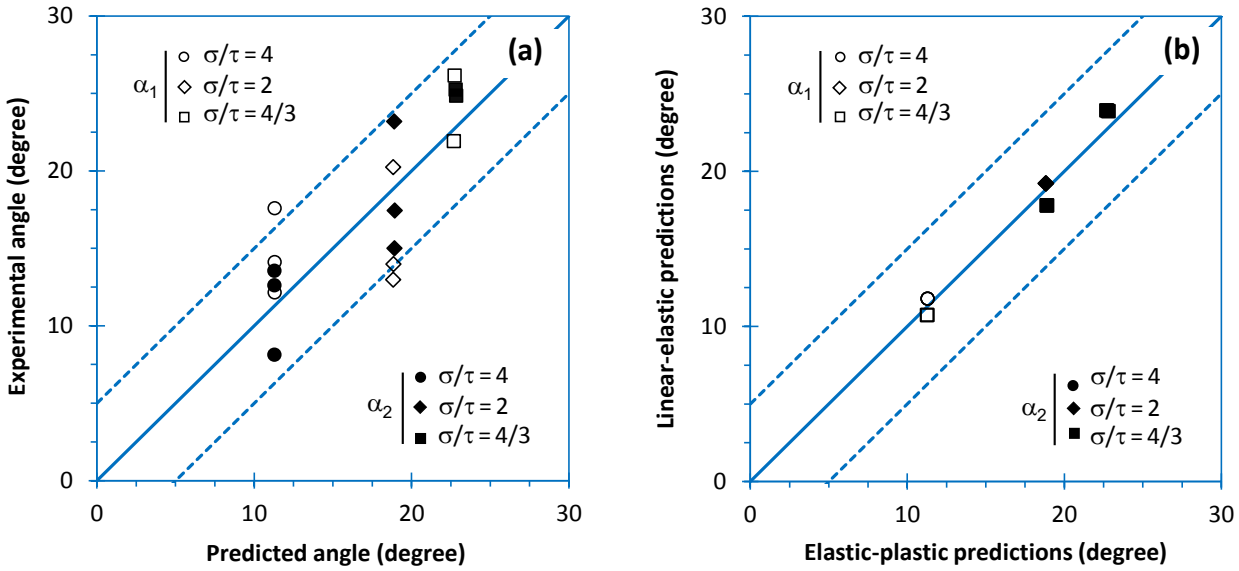

Figure 6. Comparison of crack direction: (a) elastic-plastic predictions versus experimental observations; and (b) elastic-plastic predictions versus linear-elastic predictions.

Similar to the previous case, both the elastic-plastic and the linear-elastic approaches have shown identical predictive capabilities with regard to the direction of crack at the early stage of growth. Figure 6(b) compares the numerical values obtained with the two constitutive models for the studied cases. As can be seen, the results are very-well correlated for the two sides of the hole, irrespective of the normal stress to shear stress ratios, with maximum

differences lower than 1.3°. Note that linear-elastic and elastic-plastic predictions for the same bending-torsion ratio were similar for the different loading levels, see Table 4, which explains the smaller number of data points shown in the figure. This is an interesting conclusion in a practical fatigue design perspective, because the complexity associated with the numerical modelling and the computational time of the two approaches is substantially different, but the final results are similar.

Based on the numerical simulations, it can be hypothesised that the crack initiation sites are located at the wall surface of the hole, near the outer diameter (see Figure 7). Their positions vary with the loading case and tend to move to the inner part, as the normal stress to shear stress ratio decreases. The examination of fracture surfaces by scanning electron microscopy provided support for this reasoning. In fact, the cracks initiated at the wall of the hole (see the dashed lines) from un-melted regions, mainly caused by lack of fusion or inadequate penetration, which has been identified in the literature as the main causes of fatigue crack initiation in maraging steels processed by laser beam powder bed fusion [12,23,31].

Regarding the crack initiation sites, although there is not a perfect match between the predicted ones and the experimental observations, we can see that the results are relatively close. On the other hand, it is reasonably to argue that the defects introduced by the additive manufacturing process strongly changed the stress-strain fields, acting as local stress raisers, and moving the crack initiation site to a different location in the neighbourhood of the predicted point. Figure 7 also compares the crack initiation sites predicted with the elastic-plastic (red arrows) and the linear-elastic (white arrows) models. It is worth to note that the two numerical approaches allow to obtain similar results with no significant differences. In general, the elastic-plastic predictions are shifted slightly to the outer part of the wall.

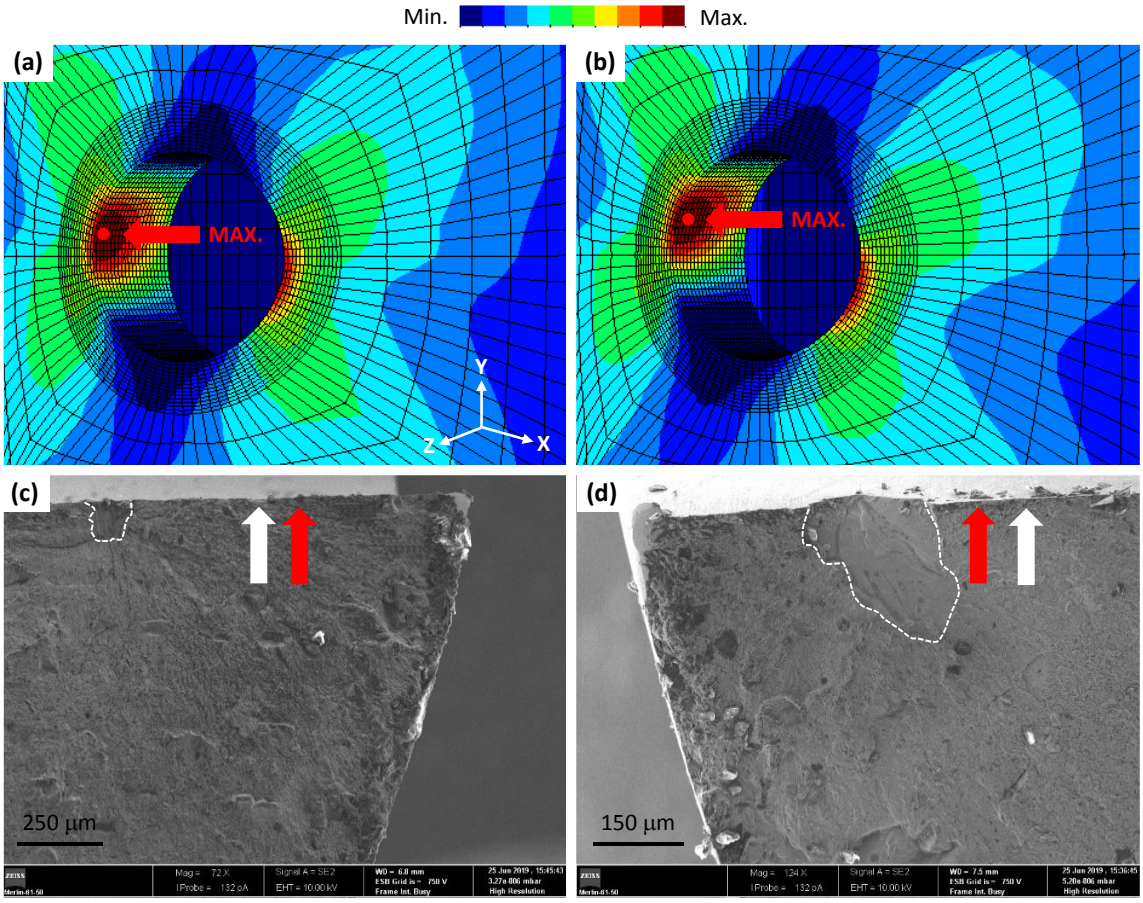

Figure 7. First principal stress fields obtained with the elastic-plastic constitutive models for: (a) $\sigma/\tau = 4$; and (b) $\sigma/\tau = 2$. Scanning electron micrographs of fracture surfaces near the hole surface: (c) $\sigma/\tau = 4$; and (d) $\sigma/\tau = 2$. Red and white arrows represent the crack initiation sites determined from the elastic-plastic and the linear-elastic constitutive models, respectively.

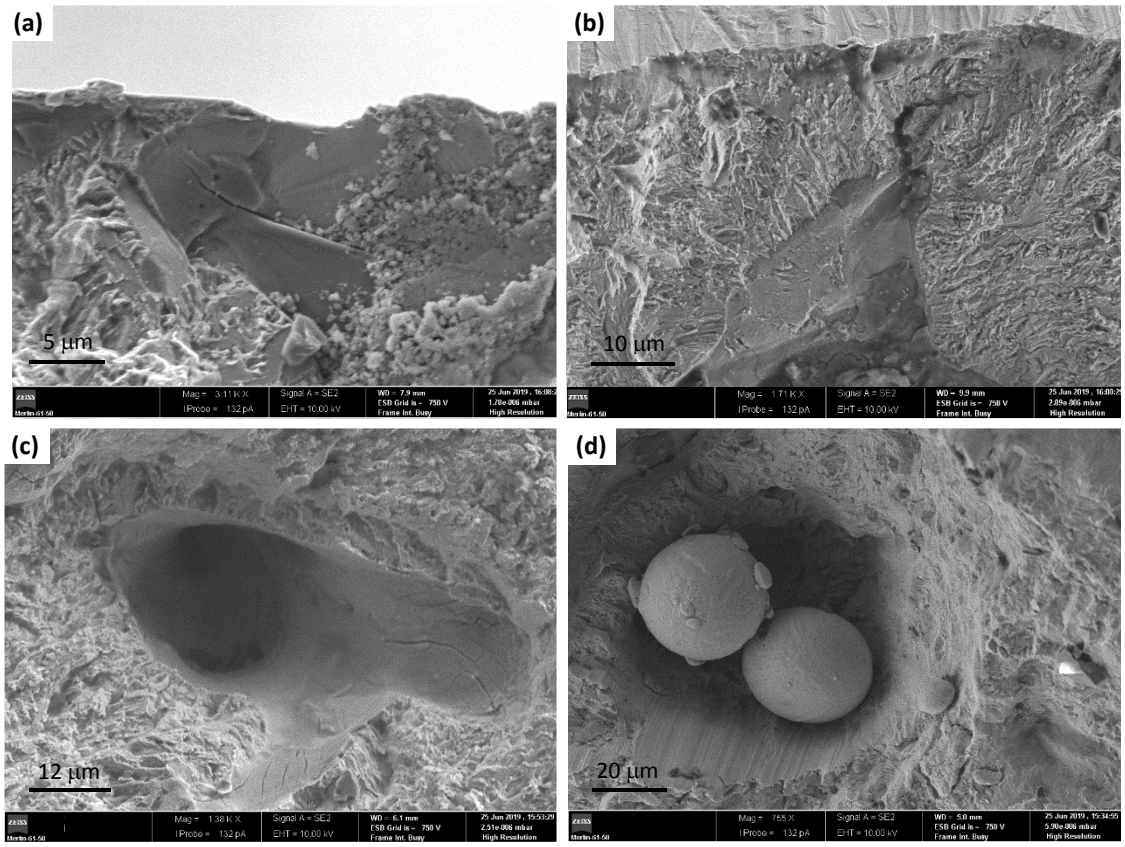

Figure 8. Examples of processing defects found at the fracture surfaces in the SEM analysis: (a) lack of fusion at surface; (b) lack of fusion at sub-surface; (c) internal void; and (d) internal void and un-melted powder particles.

The analysis of SEM micrographs with high magnification, as can be seen in Figure 8, has shown the presence of different types of voids and un-melted powder particles throughout the fracture surfaces. Although the outer surface of the samples has been machined and polished, which significantly reduced the surface roughness and also the notch effect, remnant sub-surface defects, located close the surface, were also found (see Figure 8(a) and Figure 8(b)). These defects may play an important role in the fatigue crack nucleation mechanisms and, naturally, they are also associated with the entire fatigue process.

It is was also concluded from the SEM analysis that the families of voids and un-melted powder particles exist throught the fracture surfaces but have quite different shapes, sizes, and distributions, which is a specificity of the laser beam powder bed fusion process. Despite the inner

defects can affect the fatigue behaviour, defects closer to the outer surface tend to be more detrimental. This is because the crack nucleation is generally associated with the locations of higher cyclic plastic deformation. Thus, surface and sub-surface defects, due to the plane stress state condition, are subjected to more plastic deformation. In addition, since these defects are closer to the surface, they have a greater chance to cause failure, because there is a shorter distance towards an open surface.

4.2. Stress-strain response at the notch region

An accurate evaluation of the stress-strain response at the notch region is fundamental to ensure reliable fatigue life predictions. In this study, as stated in Section 3, the nonlinear finite-element simulations were performed by applying five loading cycles. This number of loading cycles, which was optimised in a previous study [21] focused on a conventional high-strength steel, aimed at attaining a stabilised cyclic stress-strain response of the material. For the conventional high-strength steel, the analysis was carried using the strain energy density and the energy variations between the first and the fifth cycles were lower 0.4% [21].

Figure 9~~8~~ plots, as an example, the variations of the normal stress range $\Delta\sigma_{YY}$ and the shear stress range $\Delta\tau_{XY}$ at the crack initiation site with the number of applied cycles for the different loading cases. It is clear that $\Delta\sigma_{YY}$ (see Figure 9~~8~~(a)) and $\Delta\tau_{XY}$ (see Figure 9~~8~~(b)) do not suffer significant changes during the loading cycles of the numerical simulations and, therefore, the stabilised response is achieved at an early stage. Moreover, as expected, at the same normal stress to shear stress ratio, the higher is the load level, the higher are the local $\Delta\sigma_{YY}$ and the $\Delta\tau_{XY}$ stress components.

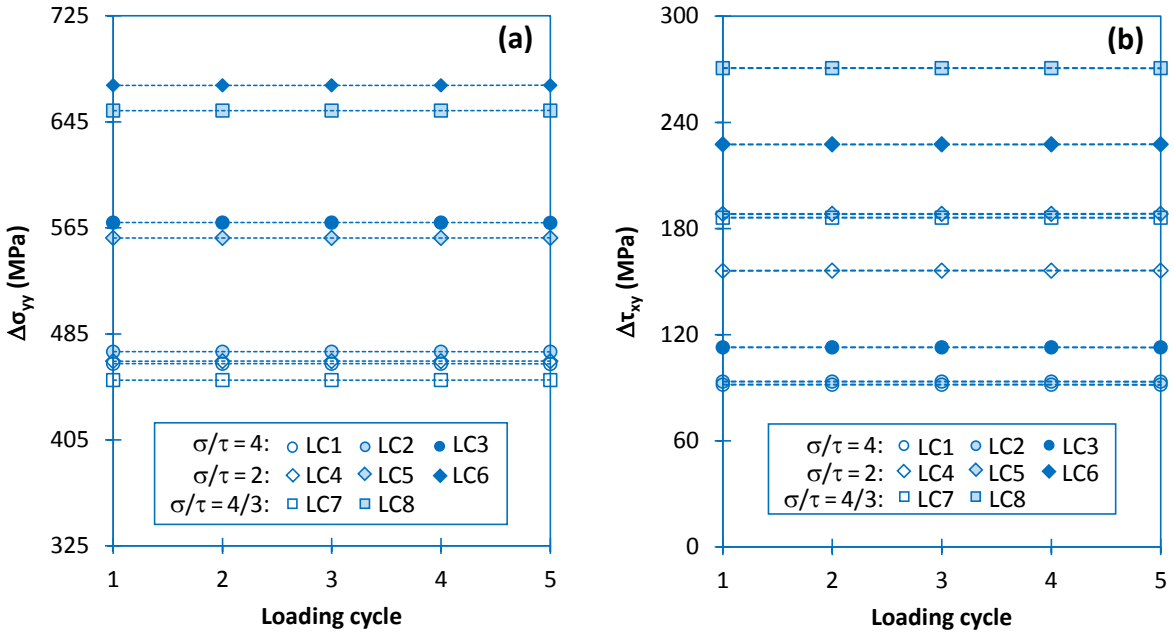

Figure ~~9~~8. Variation of the: (a) normal stress range $\Delta\sigma_{YY}$ and the (b) shear stress range $\Delta\tau_{XY}$ with the number of cycles at the crack initiation sites for the different loading cases.

Based on the simulations performed for the fifth cycle, which was selected in this study for fatigue assessment, we can characterise the stabilised stress-strain response at the notch region. Figure ~~10~~9(a) and Figure ~~10~~9(b) plot the typical profiles of the maximum von Mises stress (σ_{vM}) and the maximum von Mises strain (ε_{vM}) for the peak load along a straight line emanating from the crack initiation site in a direction normal to the hole surface. The stress is maximum at the hole surface and then diminishes progressively to an asymptotic value, where the notch effect is no longer acting. As far as the strain is concerned, the conclusions are basically the same, i.e. the maximum occurs at the surface and then we decrease towards an asymptotic value which depends on the magnitude of the applied loading.

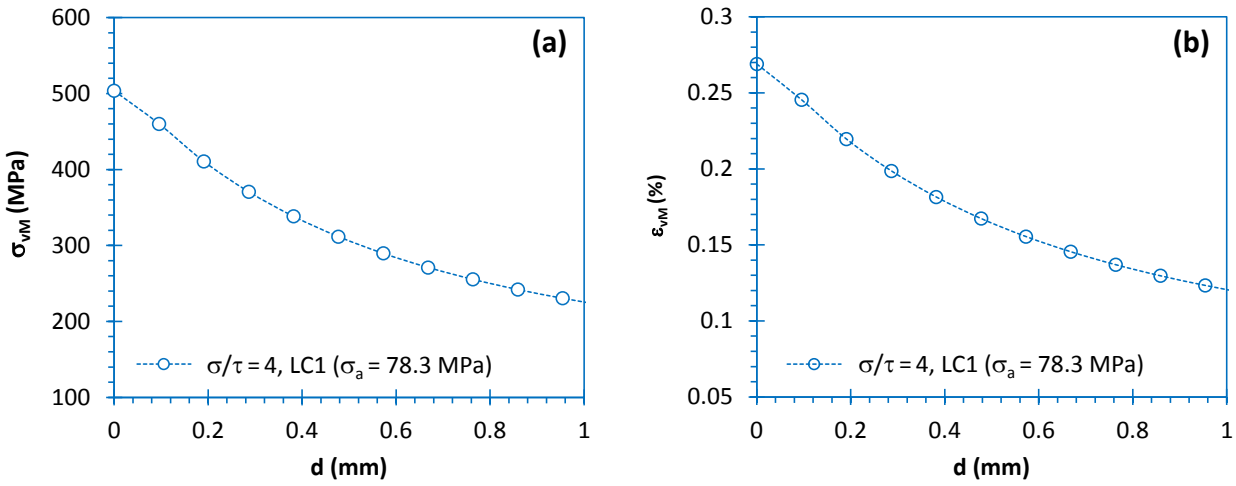

Figure 10~~9~~. Evolution of (a) von Mises stress and (b) von Mises strain with the distance from the crack initiation site along a straight line normal to the hole surface for the peak load.

In a dimensionless form, the stress and strain profiles are not significantly affected by the loading scenario. For the sake of comparability, several selected cases are displayed in Figure 11~~0~~(a) and Figure 11~~0~~(b). The von Mises stress and the von Mises strain were divided by the maximum values; and the distance from the crack initiation site was divided by the material characteristic length (a_0). Overall, the dimensionless functions are overlapped in the entire range, evidencing reduced effect of the loading case. This behaviour has already been reported in previous papers for the dimensionless stress distributions computed with linear-elastic models considering the same loading cases [12].

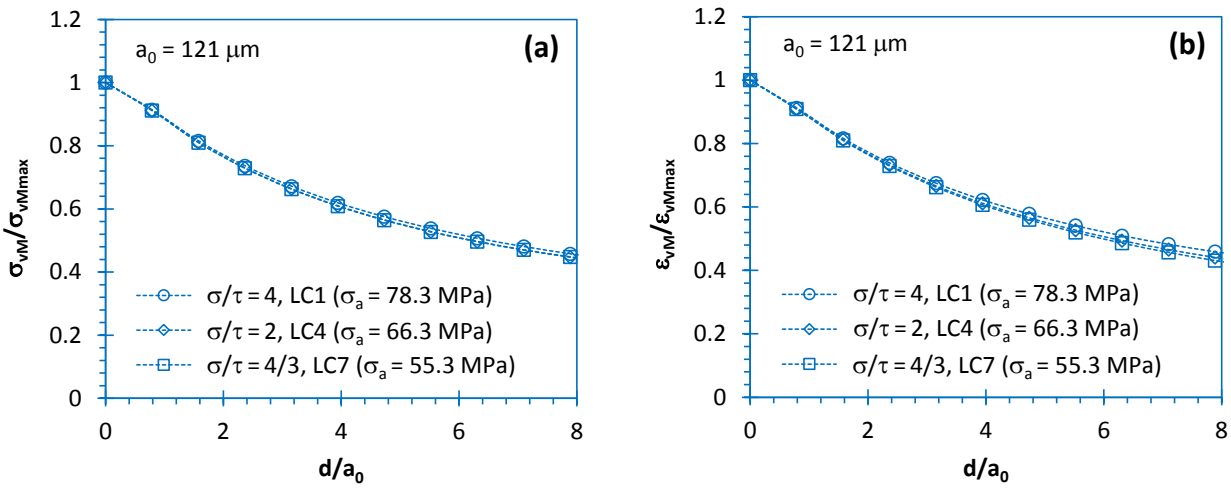

Figure 1~~0~~. Evolution of (a) dimensionless von Mises stress and (b) dimensionless von Mises strain with the normalised distance from the crack initiation site along a straight line normal to the hole surface for the peak load.

4.3. Fatigue life assessment

The fatigue life assessment was carried out using a model based on the Smith-Watson-Topper (SWT) damage parameter (see Fig. 1~~2~~1). The modus operandi consists of: (1) reduction of the multiaxial stress-strain state to an equivalent uniaxial stress-strain state; (2) calculation of an effective value of the SWT damage parameter at the notch-controlled process zone; and (3) estimation of fatigue lifetime using a SWT-life fatigue master curve [32-33]. Here the model is applied using the elastic-plastic constitutive models. In a previous research conducted by the authors, this concept has been successfully implemented within a linear-elastic framework [12].

The reduction of the multiaxial stress-strain state to an equivalent uniaxial stress-strain state (see Figure 1~~2~~1(a)) was done by computing both the equivalent von Mises stress (σ_{vM}) and the equivalent von Mises strain (ε_{vM}) at the notch region (see Section 4.2). Regarding the effective value of the SWT parameter (see Figure 1~~2~~1(b)), it was computed using the Point Method (PM) of the Theory of Critical Distances (TCD) over a straight line emanating from the crack initiation site along the crack direction at the early stage of growth. Note that the crack initiation site was defined by α, and the direction of crack at the early stage of growth was defined by β. As demonstrated in Section 4.1, the numerical predictions were quite close to the experimental observations.

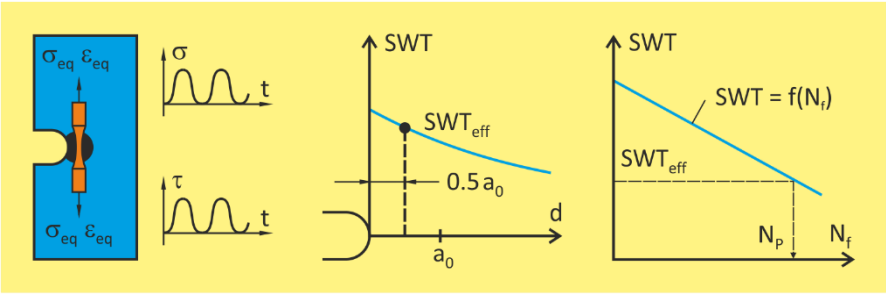

Figure 12~~1~~. Schematic presentation of the fatigue life prediction model employed in the present study: (a) reduction of multiaxial stress-strain state to an uniaxial equivalent stress-strain state; (b) calculation of an effective value of the SWT damage parameter; and (c) prediction of multiaxial fatigue life using an uniaxial SWT-based fatigue master curve.

Figure 13~~2~~(a) displays the variation of the SWT damage parameter against the distance from the crack initiation site in natural coordinates for three stress levels and the same normal stress to shear stress ratio ($\sigma/\tau = 2$). At the hole surface, the fatigue damage quantifier is maximum and then reduces progressively towards an asymptotic value. This maximum value is governed by the nominal stress level which affects not only the peak value but also the gradients of the of the SWT damage parameter at the notch-affect zone. Predictably, the peak and the asymptotic values of the SWT damage parameter increase with the increase of the nominal normal stress amplitude (σ_a). The effective values of the SWT damage parameter, represented by the dashed vertical line, are naturally affected by the loading level.

The evolution of the SWT damage parameter with the distance from the crack initiation site in normalised coordinates for the different loading cases studied here is plotted in Figure 13~~2~~(b). The values of the SWT damage parameter were divided by the maximum value, and the distance from the crack initiation site was divided by the material characteristic length (a_0). In this representation, unlike the previous figure, all functions are perfectly overlapped and follow the same trend. This means that the effective value of the SWT damage parameter occupies a fix position, i.e. approximately 95% of the peak, and that the asymptotic value is also similar for all cases, i.e. near 20% of the maximum value of the dimensionless SWT damage parameter.

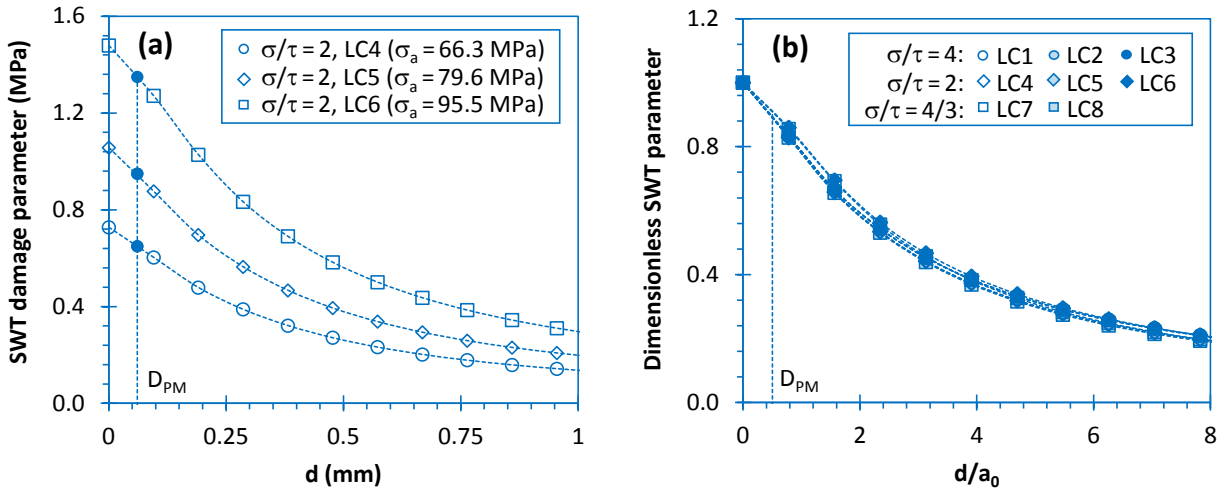

Figure 132. (a) SWT damage parameter against the distance from the crack initiation site; (b) Dimensionless SWT damage parameter against the normalised distance from the crack initiation site for different loading cases over a straight line along the direction of crack at the early stage of growth.

The effective values of the SWT damage parameter (SWT_{eff}) determined for the different loading cases using the above-mentioned procedure are summarised in Table 5. These values were inserted into the uniaxial SWT-based fatigue master curve (see Figure 121(c)) of the tested material to estimate the fatigue crack initiation life. The fatigue master curve of the additively manufactured maraging steel was determined in a previous study (see Eq. (57)) using standard smooth specimens subjected to uniaxial strain-controlled and stress-controlled conditions [12]:

$$\sigma_{max}\varepsilon_a = 10^{1.5315}\left(N_f\right)^{-0.3567} \quad (57)$$

where N_f is the number of cycles to failure. This power function is valid for both the low-cycle and high-cycle fatigue regime for $N_f < 10^6$ cycles.

The fatigue crack initiation life (N_{EP}) calculated for the tested cases from the elastic-plastic simulations is listed in Table 5. Figure 143(a) plots the predicted values against the experimental lives for the different loading cases. For the sake of comparability, scatter bands with factors of

two were plotted. As can be seen, the results are in very good agreement. The errors are relatively small, with only one point outside the scatter bands. Moreover, the predictions are distributed in a balanced way among the conservative and non-conservative regions. Overall, these trends demonstrate the high predictive capabilities of the proposed approach to assess the multiaxial fatigue lifetime in maraging steel produced by laser beam powder bed fusion.

Table 5. Effective values of the SWT damage parameter and fatigue life predictions (Point Method).

Loading case	1	2	3	4	5	6	7	8
SWT_{eff} (MPa)	0.603	0.624	0.911	0.677	0.939	1.452	0.638	1.338
N_i (cycles)	35,115	75,516	20,037	52,883	32,677	7947	84,204	8514
N_{EP} (cycles)	81,156	73,634	25,543	58,767	23,451	6912	69,214	8683
N_{LE} (cycles)	63,054	56,418	20,889	56,087	20,409	7665	54,153	8368

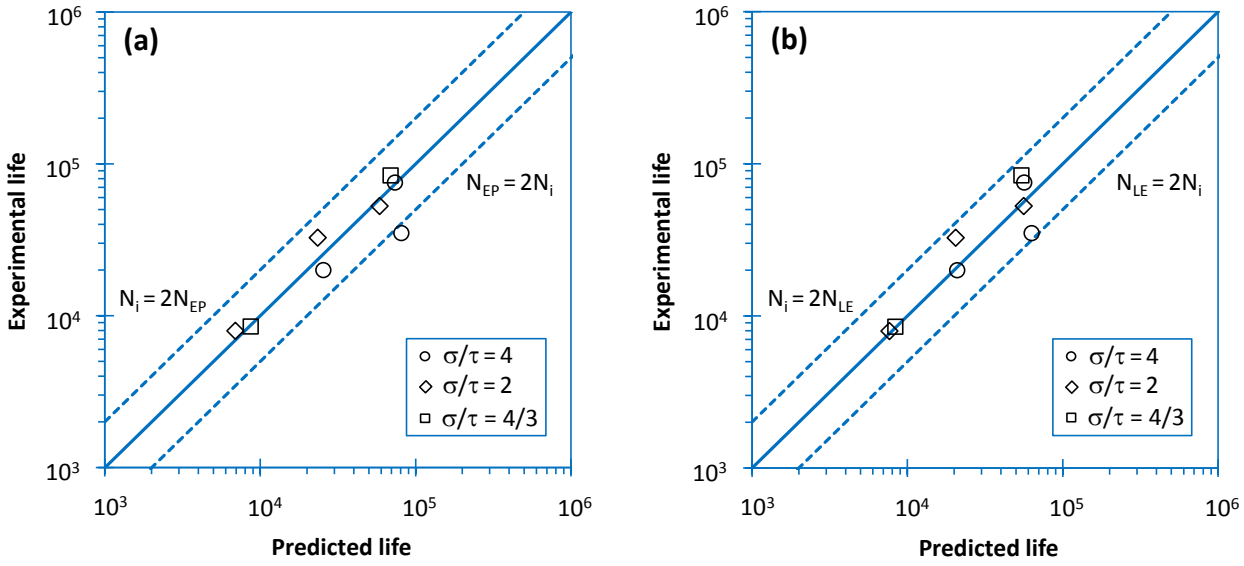

Figure 1~~4~~3. Predicted lives versus experimental lives: (a) elastic-plastic constitutive model; and (b) linear-elastic constitutive model.

The elastic-plastic predictions were compared with those obtained with the linear-elastic simulations. The linear-elastic predictions were done by using the methodology proposed by the authors in a previous paper [12]. Indeed, the methodology is rather similar to that schematised in Figure 1~~2~~1. However, prior to the determination of the effective value of the SWT parameter, the pseudo-elastic energy in the yielded zone is converted into an equivalent elastic-plastic energy using the modified Equivalent Strain Energy Density concept [34]. This energy allows the definition

of a cyclic stress-strain hysteresis loop which is used to determine the effective value of the SWT parameter. Similarly to the elastic-plastic analysis, the Point Method of the Theory of Critical Distances was used. More details about the procedure can be found in reference [12].

The fatigue crack initiation life computed with the linear-elastic models (N_{LE}) for the different loading cases is listed in Table 5. The comparison between the numerical predictions and the experimental lives (N_i) is exhibited in Figure 14(b). For the sake of comparability, scatter bands with factors of two were also plotted. It is worth to note that there is a very good agreement between the numerical and the experimental results. We can see that all points are within the scatter bands and are also balanced among the conservative and non-conservative areas. In addition, it is clear that the predictive capabilities of both approaches are relatively similar, which is an interesting finding.

In order to better evaluate the accuracy of the two tested approaches, a statistical analysis based on the probability density function of the prediction error (P_E) was conducted:

$$P_E = \mathrm{Log}\,(N_i) - \mathrm{Log}\,(N_p) \quad (6)$$

where N_i is the experimental life, and N_p is the predicted life (i.e. N_{EP} or N_{LE}). More accurate models are generally associated with lower standard deviations and mean errors closer to zero. According to Figure 15, the elastic-plastic approach led to mean errors closer to zero but slightly shifted to the non-conservative region, while the linear-elastic gave smaller standard deviations associated with predictions slightly conservative. Nevertheless, as hypothesised above, the two approaches are rather similar. In sum, the results show that both can be used in the fatigue design of maraging steel fabricated by laser beam powder bed fusion subjected to multiaxial loading.

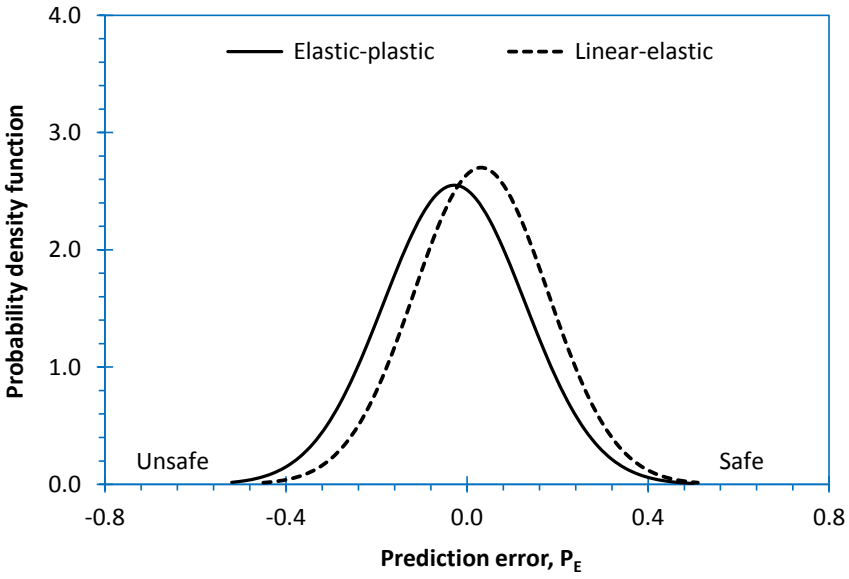

Figure 154. Probability density function of the predictive error for the approaches based on the elastic-plastic and linear-elastic constitutive models.

5. Conclusions

The present paper addressed the notch fatigue behaviour and the lifetime prediction in maraging steel manufactured by laser beam powder bed fusion subjected to proportional bending-torsion loading. Tests were conducted in tubular geometries with lateral holes considering different normal stress to shear stress ratios and multiaxial loading levels. Elastic-plastic and linear-elastic constitutive models were developed to predict the fatigue crack initiation sites, the directions of crack initiation, and the number of cycles to crack initiation. The fatigue crack initiation sites and the directions of crack initiation were determined from the first principal stress field at the hole surface, while the crack initiation life was estimated from a model based on the effective value of the SWT damage parameter evaluated at the notch-controlled process zone in conjunction with the Theory of Critical Distances. The following conclusions can be drawn:

(1) the fatigue behaviour was characterised by the initiation of two diametrically opposite cracks at the hole surface. As the normal stress to shear stress ratio decreased, the cracks tended to be closer to the transversal plane passing through the hole centre;

(2) The direction of crack initiation was governed by the loading scenario. The lower the normal stress to shear stress ratio, the higher was angle formed by the crack and the transversal plane passing through the hole centre;

(3) the crack initiation sites and the directions of crack initiation were similar for both sides of the hole, irrespective of the σ/τ ratios. Such variables were successfully predicted with nearly the same degree of accuracy using the elastic-plastic and the linear-elastic models;
(4) the generalised isotropic plasticity model with mixed isotropic-kinematic hardening demonstrated to be suitable for simulating of the cyclic plastic behaviour of maraging steel manufactured by laser beam powder bed fusion;
(5) the normalised SWT functions computed at the notch-affected process zone over a straight line along the direction of crack initiation were not affected by the loading scenario. This may explain the success of the SWT damage parameter as a robust fatigue quantifier;
(6) the SWT-based model successfully predicted the fatigue crack initiation of additively manufactured maraging steel under bending-torsion. The predictive capabilities of the elastic-plastic and the linear-elastic approaches were similar and close to the experiments.

Acknowledgment

This research is sponsored by FEDER funds through the program COMPETE – Programa Operacional Factores de Competitividade – and by national funds through FCT – Fundação para a Ciência e a Tecnologia –, under the project UIDB/00285/2020.

References

1. Socie D, Marquis G. Multiaxial fatigue. SAE International; 1999. ISBN 978-0768004533
2. Carpinteri A, Spagnoli A, Vantadori S, Viappiani D. A multiaxial criterion for notch high-cycle fatigue using a critical-point method. Eng Fract Mech 2008;75:1864–74. https://doi.org/10.1016/j.engfracmech.2006.11.002.
3. Fatemi A, Molaei R, Phan N. Multiaxial fatigue of additive manufactured metals: Performance, analysis, and applications. Int J Fatigue 2020;134, 105479 https://doi.org/10.1016/j.ijfatigue.2020.105479
4. Sanaei N, Fatemi A (2020). Defects in additive manufactured metals and their effect on fatigue performance: A state-of-the-art review. Prog Mater Sci 2020;117, 100724. https://doi.org/10.1016/j.pmatsci.2020.100724
5. Kempen K, Yasa E, Thijs L, Kruth JP, Van Humbeeck J. Microstructure and mechanical properties of selective laser melted 18Ni-300 steel. In: Physics Procedia; 2011. https://doi.org/10.1016/j.phpro.2011.03.033

6. Kürnsteiner P, Wilms MB, Weisheit A, Barriobero-Vila P, Jägle EA, Raabe D. Massive nanoprecipitation in an Fe-19Ni-xAl maraging steel triggered by the intrinsic heat treatment during laser metal deposition. Acta Mater 2017;129:52-60. https://doi.org/10.1016/j.actamat.2017.02.069
7. Tan C, Zhou K, Ma W, Zhang P, Liu M, Kuang T. Microstructural evolution, nanoprecipitation behavior and mechanical properties of selective laser melted high-performance grade 300 maraging steel. Mater Des 2017; 134:23-34. https://doi.org/10.1016/j.matdes.2017.08.026
8. Jägle EA, Choi PP, Van Humbeeck J, Raabe D. Precipitation and austenite reversion behavior of a maraging steel produced by selective laser melting. J Mater Res 2014;29:2072-2079. https://doi.org/10.1557/jmr.2014.204
9. Fayazfar H, Salarian M, Rogalsky A, et al. A critical review of powder-based additive manufacturing of ferrous alloys: Process parameters, microstructure and mechanical properties. Mater Des. 2018;144:98-128. https://doi.org/10.1016/j.matdes.2018.02.018
10. Bajaj P, Hariharan A, Kini A, Kürnsteiner P, Raabe D, Jägle EA. Steels in additive manufacturing: A review of their microstructure and properties. Mater Sci Eng A. 2020;772: 138633. https://doi.org/10.1016/j.msea.2019.138633
11. Mooney B, Kourousis K. A Review of Factors Affecting the Mechanical Properties of Maraging Steel 300 Fabricated via Laser Powder Bed Fusion. Metals (Basel). 2020;10(9):1273. https://doi.org/ 10.3390/met10091273
12. Branco R, Costa JD, Martins Ferreira JA, Capela C, Antunes FV, Macek W. Multiaxial fatigue behaviour of maraging steel produced by selective laser melting. Mater Des 2021;201: 109469. https://doi.org/10.1016/j.matdes.2021.109469
13. Carpinteri A, Spagnoli A, Vantadori S, Viappiani D. A multiaxial criterion for notch high-cycle fatigue using a critical-point method. Eng Fract Mech 2008;75:1864–74. https://doi.org/10.1016/j.engfracmech.2006.11.002.
14. Liao D, Zhu SP, Correia JA, de Jesus A, Calçada R (2018). Computational framework for multiaxial fatigue life prediction of compressor discs considering notch effects. Eng Fract Mech 2018;202:423-435. https://doi.org/10.1016/j.engfracmech.2018.08.009
15. Lutovinov M, Cerny J, Papuga J. A comparison of methods for calculating notch tip strains and stresses under multiaxial loading. Frat. ed Integrita Strutt. 2016;38:237-243.

16. Liao D, Zhu SP, Correia JAFO, De Jesus AMP, Berto F. Recent advances on notch effects in metal fatigue: A review. Fatigue Fract Eng Mater Struct. 2020;43:637-659. https://doi.org/:10.1111/ffe.13195
17. Mooney B, Agius D, Kourousis KI. Cyclic Plasticity of the As-Built EOS Maraging Steel: Preliminary Experimental and Computational Results. Appl Sci. 2020; 10(4):1232. https://doi.org/10.3390/app10041232
18. Antunes F, Santos L, Capela C, et al. Fatigue crack growth in maraging steel obtained by Selective Laser Melting. Appl Sci. 2019;9(20):4412. https://doi.org/10.3390/app9204412
19. Carpinteri A, Spagnoli A, Vantadori S (2011). Multiaxial fatigue assessment using a simplified critical plane-based criterion. Int J Fatigue 2011;33, 969–976. https://doi.org/10.1016/j.ijfatigue.2011.01.004
20. Goncalves CA, Araujo JA, Mamiya EN. Multiaxial fatigue: a stress based criterion for hard metals. Int J Fatigue 2005;27:177–87. https://doi.org/10.1016/j.crme.2004.09.003
21. Branco R, Prates PA, Costa JD, Borrego LP, Berto F, Kotousov A, Antunes FV (2019). Rapid assessment of multiaxial fatigue lifetime in notched components using an averaged strain energy density approach. Int J Fatigue 2019;124:89-98. https://doi.org/10.1016/j.ijfatigue.2019.02.005
22. McDiarmid DI. A shear stress based critical-plane criterion of multiaxial fatigue failure for design and life prediction. Fatigue Fract Eng Mater Struct, 1194;17:1475-1484 https://doi.org/10.1111/j.1460-2695.1994.tb00789.x
23. Branco R, Costa JDM, Berto F, et al. Low-cycle fatigue behaviour of AISI 18Ni300 maraging steel produced by selective laser melting. Metals (Basel). 2018;8(1):32. https://doi.org/10.3390/met8010032
24. Branco R, Prates PA, Costa JD, Berto F, Kotousov A. New methodology of fatigue life evaluation for multiaxially loaded notched components based on two uniaxial strain-controlled tests. Int J Fatigue 2018;111:308-320. https://doi.org/10.1016/j.ijfatigue.2018.02.027
25. Menezes LF, Teodosiu C. Three-dimensional numerical simulation of the deep drawing process using solid finite elements. J Mater Proc Technol 2000;97:100-106. https://doi.org/10.1016/S0924-0136(99)00345-3

26. Oliveira MC, Alves JL, Menezes LF. Algorithms and strategies for treatment of large deformation frictional contact in the numerical simulation of deep drawing process. Arch Comput Method Eng, 2008;15:113-162. https://doi.org/10.1007/s11831-008-9018-x
27. Zerres P, Bruning J, Vormwald M. Fatigue crack growth behavior of fine-grained steel S460N under proportional and non-proportional loading. Eng Fract Mech. 2010;77:1822-1834. https://doi.org/10.1016/j.engfracmech.2010.02.008
28. Luo P, Yao W, Susmel L, Li P. Prediction of fatigue damage region with the use of the notch critical plane approach for crack initiation and propagation. Int J Fatigue 2020;135:105533. https://doi.org/10.1016/j.ijfatigue.2020.105533
29. Reis L, Li B, Freitas M. Crack initiation and growth path under multiaxial fatigue loading in structural steels. Int J Fatigue 2009;31:1660–8. https://doi.org/10.1016/j.ijfatigue.2009.01.013.
30. Rozumek D, Marciniak Z, Lesiuk G, Correia JAFO, De Jesus AMP. Experimental and numerical investigation of mixed mode I+II and I+III fatigue crack growth in S355J0 steel. Int J Fatigue 2018;113:160-170. https://doi.org/10.1016/j.ijfatigue.2018.04.005
31. Meneghetti G, Rigon D, Gennari C. An analysis of defects influence on axial fatigue strength of maraging steel specimens produced by additive manufacturing. Int J Fatigue. 2019;118:54-64. https://doi.org/:10.1016/j.ijfatigue.2018.08.034
32. Correia J, Apetre N, Arcari A, et al. Generalized probabilistic model allowing for various fatigue damage variables. Int J Fatigue 2017;100:187-194. https://doi.org/10.1016/j.ijfatigue.2017.03.031
33. Cruces AS, Lopez-Crespo P, Bressan S, Itoh T, Moreno B. On the Behaviour of 316 and 304 Stainless Steel under Multiaxial Fatigue Loading: Application of the Critical Plane Approach. Metals 2019;9:978 https://doi.org/10.3390/met9090978
34. Ye DY, Matsuoka S, Suzuki N, Maeda Y. Further investigation of Neuber's rule and the equivalent strain energy density (ESED) method. Int J Fatigue 2004;26:447-455. https://doi.org/10.1016/j.ijfatigue.2003.10.002